Doctorate Dissertation

博士論文

Theoretical study on anion-doping induced metal-insulator transition of metal oxides (アニオンドープによる金属酸化物の金属絶縁体転移に関する理論的研究)

A Dissertation Submitted for Degree of Doctor of Philosophy

December 2018

平成 30 年 12 月博士(理学)申請

Department of Chemistry, Graduate School of Science,

The University of Tokyo

東京大学大学院理学系研究科化学専攻

Yuji Kurauchi

倉内　裕史

Doctorate Dissertation

博士論文

Theoretical study on anion-doping induced metal-insulator transition of metal oxides (アニオンドープによる金属酸化物の金属絶縁体転移に関する理論的研究)

A Dissertation Submitted for Degree of Doctor of Philosophy

December 2018

平成 30 年 12 月博士(理学)申請

Department of Chemistry, Graduate School of Science,

The University of Tokyo

東京大学大学院理学系研究科化学専攻

Yuji Kurauchi

倉内　裕史

Abstract

1. Introduction

Synthesis and characterization of anion-doped transition metal oxides are an active research topic in recent years. Among changes in physical properties caused by doping, metal-insulator transition (MIT) has been attracted the interest of researchers seeking promising materials for next-generation electronic devices. However, not much progress has been made in the researches of MIT by anion doping because fabrication procedure of high-quality crystalline samples needed for transport-property measurements has not been established so far. Until now, indeed, MIT was observed only in a few anion-doped compounds which can be prepared as thin films. Moreover, some compounds lack structural information, hindering detailed discussion about the mechanisms.

In such a situation, theoretical calculation is a powerful tool to complement experimental observations. Recent calculation techniques based on the density functional theory enable us to predict crystal structures of solid-state materials with good accuracy. In addition, subsequent electronic-state calculations provide us valuable information to discuss the mechanisms of MIT. In this thesis work, I theoretically investigated the crystal structures and the mechanisms of MIT of three anion-doped metal oxides: H-doped $SrFeO_2$, $NdNiO_2F$, and $Sr_2RuO_3F_2$.

2. Insulator-to-metal transition of $SrFeO_2$ by hydrogen doping

The composition and crystal structure of H-doped $SrFeO_2$ were theoretically determined by structural sampling and total energy calculations combined with thermodynamic analysis. It was suggested that the doped hydrogen atoms exist in hydride

form (H^-) replacing lattice oxide ions. This hydride incorporation resulted in electron doping and changed the occupation state of d_{zx} and d_z^2 bands of the adjacent Fe. A certain structure with a specific hydride arrangement acquired a metallic electronic state. However, thermodynamic analysis showed that such a metallic phase is meta-stable and the other structure in which the doped electrons are localized is most stable. This result suggested that H-doped $SrFeO_2$ is a mixture of an insulating matrix and percolating metallic domains, accounting for the experimental observation that the carrier density of H-doped $SrFeO_2$ was much lower than the amount of doped hydrogen.

3. Metal-to-insulator transition of $NdNiO_3$ by fluorine doping

The crystal structure of the F-doped $NdNiO_3$ ($NdNiO_2F$) was determined by exhaustive structure sampling. It was found that the fluorine atoms favor a two-dimensional *cis*-type configuration. The structure optimization including epitaxial strain and subsequent electronic state calculation reproduced both the experimental out-of-plane lattice constant and the insulating state of $NdNiO_2F$. The detailed analysis using density of states (DOS) for 3*d* electrons showed that the Ni^{2+} ion in $NdNiO_2F$ has $e_g^{\uparrow\uparrow}$ *d*-electron configuration. This configuration has a strong tendency to form insulating band structures because strong Coulomb repulsion precludes electron hopping through the $e_g^{\uparrow\uparrow}$ array. In contrast, Ni^{3+} in $NdNiO_3$ has $e_g^{\uparrow}$ configuration which allows electronic conduction. Therefore, I concluded that the change in occupation state of the e_g orbitals by fluorine doping is the trigger of MIT.

4. Metal-to-insulator transition of Sr_2RuO_4 by fluorine doping.

The experimental lattice constants and the insulating state of $Sr_2RuO_3F_2$ were theoretically reproduced by assuming the same structure as $Sr_2TiO_3F_2$. The DOS

calculation for Sr_2RuO_4 and $Sr_2RuO_3F_2$ revealed that the *d* electron configuration of Ru^{4+} (d^4) changed from $(xy, yz, zx)^4$ to $(xy)^{\uparrow}(yz, zx)^{\uparrow\uparrow}(3z^2-r^2)^{\uparrow}$ by fluorination. Accordingly, occupation number per band also changed from non-integer 4/3 to integer 1, resulting in the metal-insulator transition. The occupation of the $3z^2-r^2$ orbital in $Sr_2RuO_3F_2$ was attributed to the change in crystal field around Ru. Sr_2RuO_4 has almost regular RuO_6 octahedra and well separated t_{2g} and e_g orbitals. As a result, all the four *d* electrons occupy the lower t_{2g} band. On the other hand, $Sr_2RuO_3F_2$ has RuO_5F octahedra with long Ru–F bonds and the resulting square pyramidal crystal field stabilizes the $3z^2-r^2$ orbital.

5. Conclusion

In my thesis work, I studied metal-insulator transitions induced by anion doping by theoretical calculations. The calculation of H-doped $SrFeO_2$ revealed that the doped hydrogen exists as hydride, and the experimental carrier density could be explained by a two-component model with different electron trapping characters. In case of $NdNiO_2F$, I found the change in occupation state of e_g orbitals triggers MIT. The last investigation of the redox-neutral transition between $Sr_2Ru^{4+}O_4$ and $Sr_2Ru^{4+}O_3F_2$ demonstrated that the transitions is caused by modification of crystal field associated with anion substitution. These new knowledges of metal-insulator transitions would provide a new perspective to design functional anion-doped compounds in further researches.

Acknowledgements

First of all, I'm deeply grateful to my supervisor, Prof. Tetsuya Hasegawa. He provided me with a wonderful environment for theoretical studies. His advice was always incisive and fruitful to improve my research skills. This work would not have been possible without his persistent help. My deepest appreciation goes to Dr. Hideyuki Kamisaka who patiently helped my daily research activity. I was always impressed with his rich and precise knowledge of physics and computational science. I owe my skills in theoretical researches to his tremendous supports. I owe a very important debt to Prof. Akira Chikamatsu and Prof. Tsukasa Katayama. Their advice from a standpoint of experimentalists was greatly helpful to plan my researches and prepare presentations for conferences. All the studies in this thesis had started with research discussion with them. I would also like to express my gratitude to Prof. Tomoteru Fukumura, Prof. Yasushi Hirose, Dr. Shoichiro Nakao, Mrs. Mie Unimo, Mrs. Miki Komazawa, and Mrs. Aya Imoji for their beneficial comments and encouragements for my research life in Hasegawa laboratory.

Special thanks to the current and former members of Kamisaka group and Chikamatsu/Katayama group, Dr. Anri Watanabe, Prof. Kei Shigematsu, Dr. Shungo Kojima, Dr. Thantip S. Krasienapibal, Prof. Mayuko Oka, Dr. Tomoya Onozuka, Mr. Naoaki Hashimoto, Mr. Koki Kawahara, Mr. Keisuke Yamada, Mr. Yusuke Suzuki, Mr. Toru Koizuki, Mr. Takahiro Maruyama, Mr Takaaki Shiina, Mr Shishin Mo, Mr Takuto Wakasugi, Mr. Ken Hayahara, Mr. Kuni Yamada, Mr. Gu Ke, Mr. Ryota Ishigami, Mr. Kento Magara, Mr. Jun Kasahara for their valuable comments in weekly meetings. I also

appreciate every feedbacks of the other members of Hasegawa laboratory. I especially thank contemporary of mine, Mr. Yutaka Uchida, Mr. Keisuke Kawahara, Mr. Ryota Kantake, Mr. Dai Kutsuzawa, Mr. Fahd Khan Sikander, and Mr. Takanori Yamazaki.

I was supported by Advanced Leading Graduate Course for Photon Science (ALPS), providing me with scholarship and a variety of valuable programs for my doctoral course. Special thanks to Prof. Atsushi Fujimori in the Department of Physics for continuing support as a sub-supervisor in the ALPS course.

The computations were partially performed using Research Center for Computational Science, Okazaki, Japan.

Finally, I would like to express a deep appreciation to my family and friends for their warm support.

December 2018

Yuji Kurauchi

Contents

Chapter 1. General introduction

1.1. Synthesis of anion-doped transition metal oxides

Over the years, synthesis and characterization of transition metal oxides (TMO) have been occupied the interest of researchers in the field of materials science. This is not only because the number of transition metal elements is simply large, but also because transition metal oxides exhibit abundant physical properties such as magnetism, ferroelectricity, superconductivity and metal-insulator transition [1]. These properties are categorized as collective phenomena: microscopic state of each atom changes simultaneously over the whole crystal. Resultant macroscopic physical properties and their drastic responses to external stimuli, such as electric field, make transition metal oxides promising materials for electronic devices.

In this research field, doping is the most basic concept to obtain new materials and modulate the physical properties of original transition metal oxides. A conventional method is cation substitution. This chemical manipulation is employed for mainly two purposes. One is carrier doping or reduction/oxidation of cations, which can be achieved by aliovalent substitution. For example, substituting Sr^{2+} for existing La^{3+} in La_2CuO_4 generates excess holes and enhances the conductivity, finally resulting in emergence of superconductivity as follows [2]. While the precursor copper oxide is an antiferromagnetic insulator, the Sr substitution makes the system metallic. With an optimal concentration of Sr (~ $La_{1.8}Sr_{0.2}CuO_4$), the material shows superconductivity with the critical temperature T_c up to ~ 40 K. Another effect of cation doping is structural distortion associated with doping of cations with different ionic radii. Figure 1-1 shows

crystal structures of $CaTiO_3$ and $SrTiO_3$ which are good examples indicating how the size of constituent cations affects the structures. $SrTiO_3$ has a simple cubic crystal system because the constituent cations and anion have ideal ionic radii to construct the perovskite structure. Meanwhile, $CaTiO_3$ has a distorted structure due to the smaller ionic radius of Ca. A structural change can also cause changes in physical properties. For example, lattice distortion induced by substitution of larger Ba in $SrTiO_3$ results in emergence of ferroelectricity [3].

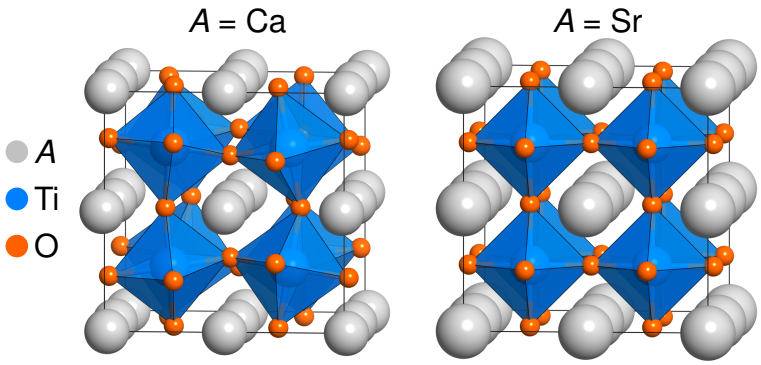

Figure 1-1. Structural deviation of a perovskite titanium oxide $ATiO_3$ according to the ionic radii of the *A*-site cation. This and following images of crystal structures are drawn by VESTA [4].

In this few decades, another approach, anion doping, has been established, and an increasing number of so-called mixed-anion oxides, in which oxide anion (O^{2-}) and other anionic species such as H^-, N^{3-}, and F^- coexists, have been synthesized [5,6]. Doped anions can not only substitute for lattice oxide ions but also be inserted into interstitial sites (Figure 1-2(a)). Moreover, anion substitution brings a coordination degree of freedom which plays an important role in coordination chemistry (Figure 1-2(b)). Therefore, anion-doped products are expected to show a variety of possible structures and corresponding physical properties.

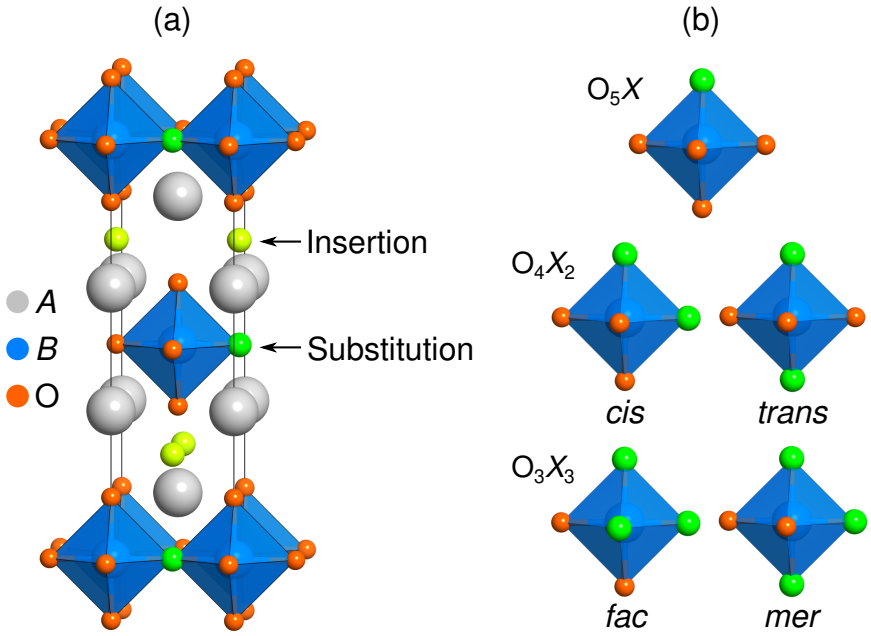

Figure 1-2. Schematic images of anion doping to oxides with a perovskite-related structure. (a) Anion substitution and insertion to a layered perovskite structure A_2BO_4. (b) Possible coordination states of a octahedral unit BO_mX_n in anion-doped perovskite oxides.

Until recently, it had been difficult to synthesize mixed-anion materials because they are often meta-stable and tend to decompose into more stable single-anion compounds at high temperatures. It is unlikely to obtain mixed-anion materials by the conventional solid-state reaction, namely "shake-and-bake" processing, performed at high temperature around 1000 K. Recent success in synthesis of mixed-anion oxides has been achieved by employing new processing techniques where low temperature or high pressure is utilized so that meta-stable phases can be realized. In the following sections, I review recent achievement in synthesis of mixed-anion transition metal oxides. I focus on hydride (H^-) and fluorine (F^-) doping to perovskite-related structures which are closely related to my research targets.

1.1.1. Hydride doping

Hydrogen is an amphoteric element taking opposite ionic states, proton (H^+) and hydride (H^-), besides the neutral molecular form (H_2). Because hydrogen is a ubiquitous element existing as moisture in air, it is easily intercalated into oxides as unintentional defects. Speaking of chemical state of hydrogen in oxides, it is a common sense that hydrogen immediately makes a bond with lattice oxygen and exists as proton (H^+) or hydroxide anion (OH^-). Indeed, theoretical works proposed that interstitial hydrogen in the zinc oxide exists as proton near the lattice oxygen [7,8]. Hydride (H^-) state is also possible in metal oxide [8]. In that case, hydride is located at the lattice oxygen site. Anyway, researches of hydrogen in oxides have been often motivated by unintentional or even undesired degradation of materials caused by H^+ or H^- defects. For example, theoretical studies of hydrogen in zinc oxides were intended to elucidate the origin of unintentional *n*-type conductivity [7,8].

Researches of "intentional" doping of hydrogen, especially hydride, of which concentration is far beyond defect level was initiated with the development of a soft chemical synthesis method. In this method, a precursor oxide and metal hydride salt such as CaH_2 are heated at temperature from 250 °C to 600 °C. This modest temperature is enough for CaH_2 to react with oxides but can suppress the decomposition of hydride-doped products (oxyhydrides). In addition, the framework of precursor oxides is preserved in the reaction because cations are less mobile at such low temperature. As a result, the precursor and the oxyhydride have similar crystal structures, making it easy to discuss the effects of hydride doping on physical properties. This type of reaction keeping crystal structures is called "topotactic" or "topochemical" reaction. A leading example of

topotactic hydride doping to perovskite-related transition metal oxide is $LaSrCoO_3H_{0.7}$ reported in 2002 [9]. This cobalt oxyhydride was synthesized by reaction of $LaSrCoO_4$ with CaH_2 at 450 °C. Using the same methodology, Ti- [10–12], V- [13], and Co-based [9,14] oxyhydrides have been synthesized so far.

Recent few years witnessed establishment of another type of reaction process using high-pressure and high-temperature. This method was inspired by high-pressure synthesis of transition-metal hydride $LiNiH_3$ and $CaPdH_3$ with perovskite structure [15,16]. It was found that formation of complex metal hydrides requires high temperatures although hydrides usually decompose to metal and hydrogen gas (H_2) at such high temperatures. To solve this conflict, high pressure was utilized to suppress H_2 gas emission and to stabilize the solid hydride phases. In addition, perovskite-related structures are relatively dense or have close-packed structure. Therefore, it is reasonable to apply high pressure to obtain perovskite materials in terms of reaction enthalpy. Synthesis of oxyhydrides under high-temperature and high-pressure follows this strategy. The first example is $SrCrO_2H$ reported in 2014 [17]. In contrast to topotactic reaction, the starting materials are far from perovskite: SrO, SrH_2, and Cr_2O_3. Nonetheless, reaction at 5 GPa and 1000 °C produces perovskite $SrCrO_2H$. Similarly, Sc [18] and Mn [19] oxyhydrides have been achieved by this strategy.

Table 1-1 summarizes perovskite-related transition-metal oxyhydride obtained by the topotactic reaction and the high-pressure reaction. Materials exploration of 3*d* transition metal-based oxyhydrides is almost completed although copper oxyhydrides have not been synthesized yet.

Table 1-1. Transition metal oxyhydrides with perovskite-ralated structures. All the reactions were performed in powder form unless otherwise noted.

Product	**Reaction method**	**Change in average valence**	**Ref.**
$BaScO_2H$	High-pressure	$Sc^{3+} \rightarrow Sc^{3+}$	[18]
$ATiO_{3-x}H_x$ (A = Ca, Sr, Ba)	CaH_2 (powder & film)	$Ti^{4+} \rightarrow Ti^{(4-x)+}$	[10,11,20]
$EuTiO_{3-x}H_x$	CaH_2	$Ti^{4+} \rightarrow Ti^{(4-x)+}$	[12]
$SrVO_2H$	CaH_2 (powder & film)	$V^{4+} \rightarrow V^{3+}$	[13,21]
Sr_2VO_3H	CaH_2, High-pressure	$V^{4+} \rightarrow V^{3+}$	[13,22]
$Sr_3V_2O_3H_2$	CaH_2	$V^{4+} \rightarrow V^{3+}$	[13]
$SrCrO_2H$	High pressure	$Cr^{3+} \rightarrow Cr^{3+}$	[17]
$LaSrMnO_{3.3}H_{0.7}$	High pressure	$Mn^{1.5+} \rightarrow Mn^{2.3+}$	[19]
$SrFeO_xH_y$	CaH_2 (film)	$Fe^{3+} \rightarrow Fe^{2+}$	[23]
$SrCoO_xH_y$	CaH_2 (film)	$Co^{3+} \rightarrow Co^{2+}$	[24]
$LaSrCoO_3H_{0.7}$	CaH_2	$Co^{3+} \rightarrow Co^{1.7+}$	[9]
$Sr_3Co_2O_{4.33}H_{0.84}$	CaH_2	$Co^{3+} \rightarrow Co^{1.75+}$	[14]

Crystal structures of the oxyhydrides have been determined by Rietveld refinement using X-ray diffraction or/and neutron powder diffraction data. In all cases, insertion of hydrogen atoms does not occur. Instead, they take places of lattice oxygen, and this is one of the reasons why doped hydrogen is considered as hydride (H^-). The absence of hydride insertion can be understood by considering the nature of topotactic reactions. The topotactic reaction with CaH_2 is highly reductive. Actually, the valence of the metal cations decreases by the reactions (Table 1-1). Under such a reductive condition, hydride insertion is unlikely because it is an oxidative phenomenon. In case of high-pressure

reaction, atomic insertion and consequent lattice expansion are obviously disadvantageous.

1.1.2. Fluorine doping

Synthesis of transition metal oxyfluorides has a longer history than that of oxyhydrides. In 1962, it was found that the conventional sintering method can produce layered-perovskite oxyfluoride K_2NbO_3F from K_2CO_3, Nb_2O_5 and KF [25]. High-pressure reaction was employed in 1971 to obtain $KTiO_2F$ from TiO_2 and KF [26]. These earlier successes in synthesis of oxyfluorides than oxyhydrides can be attributed to the chemical nature of fluorine. The possible valence state of fluorine is only F^-, while hydrogen can take H^+, H_2, and H^- states. Moreover, the ionic radius of F^- (133 pm) is close to that of O^{2-} (140 pm). Therefore, incorporation of F^- into metal oxides is not so chemically challenging compared with H^- doping.

Besides the two methods mentioned above, topotactic reaction is also effective to obtain transition metal oxyfluoride. So far, fluorine doping can be achieved by various reagents in contrast with topotactic hydridation in which only CaH_2 has been used. The most primitive reagent is F_2 gas. Inorganic fluoride salts (CuF_2, ZnF_2, XeF_2, NH_4F) and organic polymers such as polyvinylidene fluoride (PVDF) [27] have also been utilized. In case of hydride doping, only substitution occurs because both the reductive topotactic reaction using CaH_2 and the high-pressure reaction disfavor anion insertion. On the other hand, topotactic reactions using F_2 and fluoride salts are relatively oxidative, and thus fluorine insertion is also promoted. As a result, perovskite-related oxyfluorides have much more structural variations than oxyhydrides.

Table 1-2. Transition metal oxyfluorides with the layered-perovskite structure. They are categolized according to the position of doped fluorine atoms. All the reactions were performed in powder form unless otherwise noted.

Product	**Reaction method**	**Ref.**
Substitution only		
Sr_2ScO_3F	Sintering	[28]
Sr_2FeO_3F	Sintering	[29]
Sr_2BO_3F (B = Mn, Fe, Co, Ni)	High-pressure	[30–33]
K_2NbO_3F	Sintering	[25]
Substitution & insertion		
$Sr_2TiO_3F_2$	PVDF	[34]
$La_2NiO_3F_2$	PVDF	[35]
$Ba_2ZrO_3F_2 \cdot 0.5H_2O$	NH_4F, CuF_2, ZnF_2	[36]
$Sr_2CuO_2F_{2+\delta}$	F_2	[37]
Insertion only		
$LaSrMnO_4F_{1+\delta}$	F_2	[38]
Unknown		
$Sr_2RuO_3F_2$	PVDF (film)	[39]

Table 1-2 summarizes results of fluorine doping to transition metal oxides with layered-perovskite structure A_2BO_4. This structure accepts both anion substitution and insertion (Figure 1-2(a)). As a result, oxyfluorides have different crystal structures according to which type of reaction method was employed. For example, high-pressure reaction always results in oxyfluorides with substituted fluorine atoms (A_2BO_3F) because insertion is energetically unfavorable. On the other hand, highly oxidative reaction using

F_2 gas produces oxyfluorides in which all the fluorine atoms occupy the interstitial site ($LaSrMnO_4F_{1+\delta}$). Under the medium conditions with PVDF and fluoride salt, anion substitution and insertion can occur at the same time ($A_2BO_3F_2$), and this positional degree of freedom brings a diversity of crystal structures.

Figure 1-3 shows the crystal structure of $Sr_2TiO_3F_2$, $La_2NiO_3F_2$, and $Ba_2ZrO_3F_2{\cdot}0.5H_2O$. Among them, $Sr_2TiO_3F_2$ adopts the simplest structure in which coexistence of substitution and insertion is realized by alternating fluorine occupation of the apical oxygen sites and the interstitial sites [34]. On the other hand, the structure of $La_2NiO_3F_2$ is much more complex and beyond an empirical expectation that oxygen atoms should keep their positions as possible. In this compound, fluorine atoms replace the apical oxygen atoms, and a half of kicked-out oxygen atoms occupy the interstitial site. The ordered half occupation of the interstitial layer is accompanied with the large octahedral rotation. This unfamiliar structure was discovered most recently in 2018 [35], indicating that there might be more structural variations for layered oxyfluorides although uncovered yet. The final case, $Ba_2ZrO_3F_2{\cdot}0.5H_2O$, is exceptional because crystal water is also incorporated into the interstitial sites and the effective number of anions are larger than 5. As a result, both interstitial layers are occupied by anions. The crystal water can be removed by heating the crystal at 500 °C but detailed information of the crystal structure of dehydrated $Ba_2ZrO_3F_2$ is not known [36].

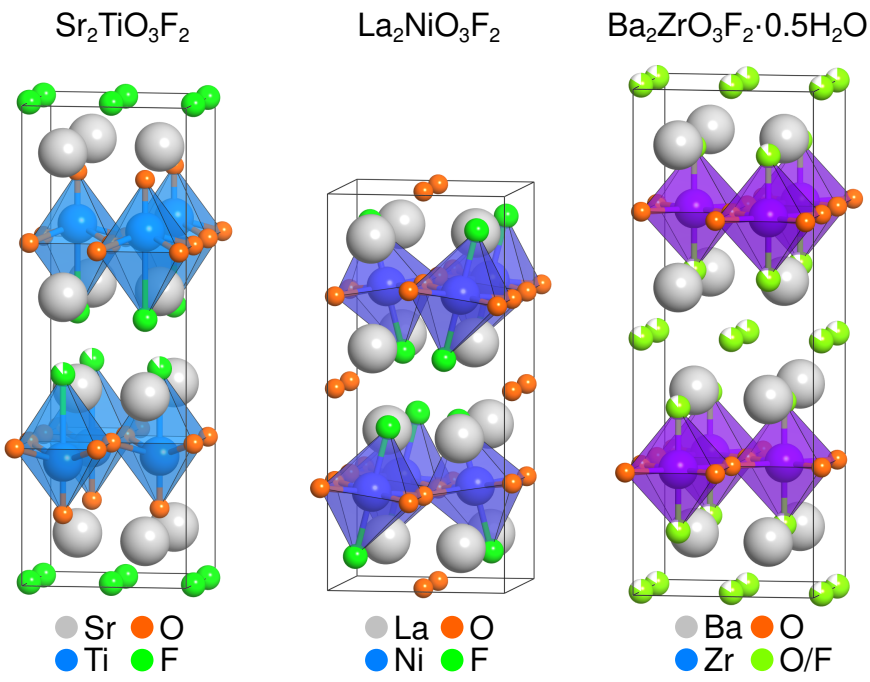

Figure 1-3. Crystal structure of $Sr_2TiO_3F_2$, $La_2NiO_3F_2$ and $Ba_2ZrO_3F_2 \cdot 0.5H_2O$

Table 1-3 summarizes oxyfluorides with the simple perovskite structure $ABO_{3-x}F_x$. In contrast to the layered perovskite, the simple perovskite does not afford fluorine insertion even with PVDF or XeF_2, suggesting that this structure is already so dense that there is no room for insertion. Most of the oxyfluorides (Sc, Ti, and $BaFeO_2F$, $PbFeO_2F$, $AgFeOF_2$, $KNbO_2F$) are classified into cubic crystal system. In the orthorhombic $SrFeO_2F$, the displacement of oxygen atoms from the ideal cubic structure is so small (0.2 Å) that there had been a debate whether $SrFeO_2F$ is cubic or orthorhombic [40–43]. Fluorine atoms in these compounds have a 3D-random distribution. As for manganese oxyfluorides, the Jahn-Teller effect of Mn^{3+} induces tetragonal distortions. However, biased fluorine distributions have not been reported.

Table 1-3. Transition metal oxyfluorides with the simple perovskite structure. All the synthesized through reactions of powder form unless otherwise noted..

Product	**Reaction method**	**Ref.**
$BaScO_2F$	Sintering	[44]
$PbScO_2F$	High-pressure	[45]
$KTiO_2F$	High-pressure	[26]
$SrMnO_{2.5-x}F_{0.5+x}$	XeF_2	[46]
$PbMnO_2F$	High-pressure	[47]
$Sr_{1-x}Ba_xFeO_2F$	PVDF (powder & film)	[40–43,48–56]
$PbFeO_2F$	High-pressure	[57]
$AgFeOF_2$	High-pressure	[58]
$NdNiO_2F$	PVDF (film)	[59]
$A NbO_2F$ (A = Li, Na, K)	Sintering	[60]

1.2. Metal-insulator transitions induced by anion-doping

Among changes in physical properties caused by doping, metal-insulator transition (MIT) is one of the most appealing phenomena because it is switching between the totally opposite fundamental states of material: metal and insulator. MIT has also drawn researchers' attention to electronic device applications. For example, resistive random access memory (ReRAM) is an emerging type of non-volatile RAM using insulating and metallic states of material as logic levels (0 and 1 for example). It is expected that ReRAM overcomes the limitation of downscaling in the current technology using transistors because of its simple architecture, where the memory cells consist of a resistivity-switching material sandwiched between electrodes [61].

Materials showing MIT and its mechanisms have been intensively studied [1]. In this subchapter, I explain the basis for understanding the mechanism of MIT in transition metal oxides and review reports of MIT induced by anion doping.

1.2.1. Possible triggers of metal-insulator transitions

In transition metal oxides, valence *d* electrons play main roles to determine their physical properties. Because *d* orbitals are localized around nuclei compared with *s* or *p* orbitals, *d*-electrons undergo strong Coulomb interaction between themselves. Such situation, called strongly electron correlation, causes various physical phenomena that cannot be explained by the classical band theory. For example, most of transition-metal oxides are insulating despite that their *d* bands are partially filled and thus they are supposed to be metallic according to the band theory. This anomalous insulating state, called Mott insulator, is a consequence of Coulomb repulsion between *d*-electrons. The

strongly correlated electronic state has been discussed using the Hubbard model. According to the Hubbard model, an electronic state is governed by two parameters, t and U, where t is the transfer integral to neighboring sites (qualitatively equivalent to band width) and U is the Coulomb repulsion between electrons at the same site (on-site Coulomb interaction). Solution of the Hubbard model depends on balance between t and U so that U/t is called correlation factor. When t is 0 (correlation factor U/t is infinity), the solution is a completely localized state where each site is occupied by immobile electrons. On the other hands, the Hubbard Hamiltonian with $U = 0$ gives an itinerate state like plane waves where electrons traverse the whole system. The Hubbard model represents competition between itinerancy (metallic) and localization (insulating) according to the U/t ratio. The Mott insulator is described as a situation where band width t of d-electrons is so small compared with the Coulomb repulsion U that the localized state wins.

An extended Hubbard model where deviation of electron number n is also included provides a useful phase diagram to consider the mechanisms of MIT in transition metal oxides. Figure 1-4 shows a map of metallic or insulating solutions derived with various combinations of the correlation factor U/t (center axis) and deviation of electron number n from a certain integer (bottom axis). According to this diagram, MIT can occur in two ways. One is called band-width controlled MIT (BC-MIT in Figure 1-4). BC-MIT is caused by enhancing or reducing the correlation factor U/t. In actual experiments, BC-MIT is observed by modifying the band width t using chemical substitutions since Coulomb repulsion U is difficult to tune as desired. Particularly, perovskite oxides ABO_3 with a transition metal at B-site is suitable to observe BC-MIT. Substitution of smaller cations for A-site causes deviation of the B–O–B bond angles from 180° (Figure 1-1).

Consequent suppression of *d-p* orbital overlap reduces the band width *t* for *d*-electrons, making the system prefer an insulating state. A typical example is metal-to-insulator transition of $LaNiO_3$ by substitution of smaller rare earth cations (Pr^{3+}–Lu^{3+}) for La^{3+} [62–69].

The other mechanism is filling-controlled MIT (FC-MIT) which is induced by deviation of electron number. For example, a Mott insulator with an integer number of electrons per site transits to a metallic phase by electron or hole doping. This FC-MIT draws an analogy between carrier doping to semiconductor. As seen in Figure 1-4, an extra electrons or holes is needed for the transition if the correlation factor *U*/*t* is high. As a result, it is often seen that the actual carrier concentration differs from that expected from the amount of dopant.

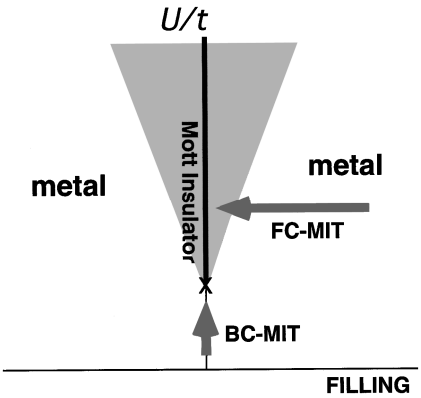

Figure 1-4. Diagram of MIT based on the Hubbard model. White and gray regions depict metallic and insulating phases, respectively. Reprinted with permission from Ref. [1]. Copyright 1998 by the American Physical Society.

In 2000, another type of MIT which cannot be categorized to BC nor FC was observed by Sr doping to a layered perovskite ruthenium oxide Ca_2RuO_4 [70,71]. While pristine Ca_2RuO_4 is an insulator below 357 K [72], replacing 1/4 of Ca results in a metal in a whole temperature range. Theoretical calculations suggested that change of crystal

field splitting and consequent rearrangement of *d*-electrons cause this insulator-to-metal transition [71]. Figure 1-5 shows schematic diagrams of d^4 configurations in the end materials: insulating Ca_2RuO_4 and metallic Sr_2RuO_4. In the case of Ca_2RuO_4, the t_{2g} levels are split into lower *xy* and higher *xz, yz* because RuO_6 octahedra are compressed along the *z*-axis. As a result, the fourth electron occupies the separated down-spin *xy* orbital. In this electronic configuration, the electron number of each orbital is one. Due to this integer occupation and Coulomb repulsion *U* between *d*-electrons, Ca_2RuO_4 is a Mott insulator. On the contrary, Sr_2RuO_4 has elongated octahedra along the *z*-axis. This opposite distortion brings about the opposite crystal field splitting. As a result, Sr_2RuO_4 has one electron in degenerated (*xz*, *yz*) orbitals. These quarter-filled *xz* and *yz* orbitals contribute to the metallic conductivity of Sr_2RuO_4.

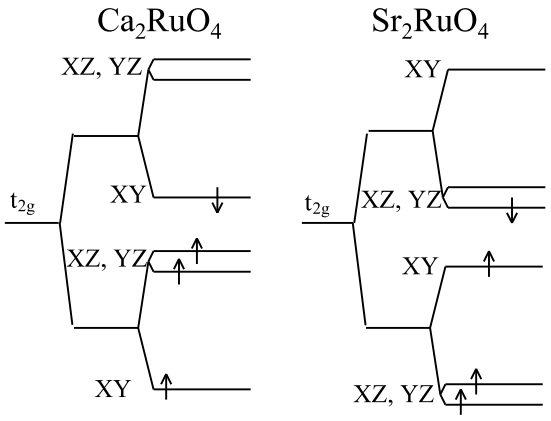

Figure 1-5. Schematic diagrams of d^4 configurations in insulating Ca_2RuO_4 and metallic Sr_2RuO_4. The six t_{2g} orbitals are firstly divided into majority- and minority-spin orbitals and then split into *xy* and degenerate *xz*, *yz* orbitals by the crystal field. Adapted by permission from Springer Nature: EDP Sciences, Eur. Phys. J. B [71], copyright by EDP Sciences, Springer-Verlag 2002.

Among the three mechanisms of MIT (BC, FC, and crystal field switching), the latter two are possible triggers of MIT by anion doping as shown in Figure 1-6. Firstly, FC-MIT can be induced by aliovalent anion substitution and anion insertion because these manipulations change electron number of transition metal cations. Specifically, substituting H^- or F^- for existing O^{2-} gives excess electrons, and insertion of any anionic species brings holes (Figure 1-6(a)). Secondly, MIT induced by crystal field switching is also possible in anion-doped systems. Anion substitution causes additional crystal field splitting because it breaks the local symmetry of the original crystals (Figure 1-6(b)). This may change the electronic configuration of transition metal cations and thus the conductivity of the system.

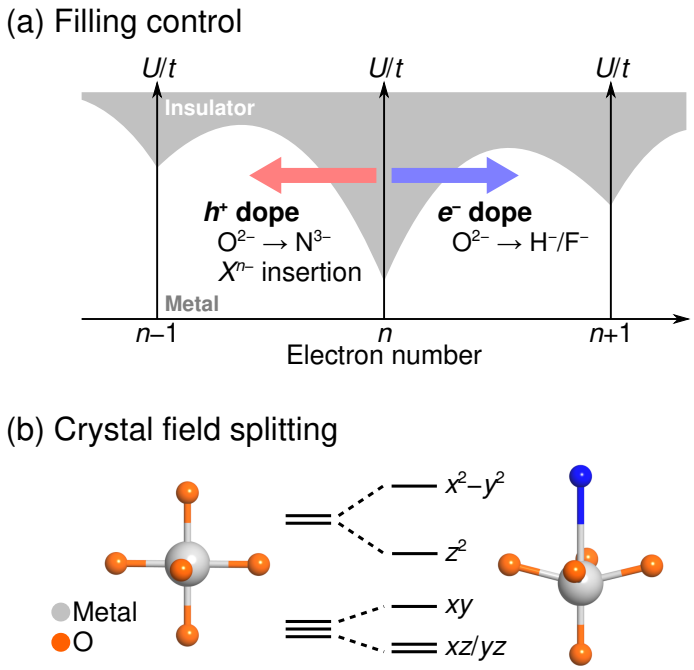

Figure 1-6. Possible triggers of MIT by anion doping. (a) Filling control by substitution of aliovalent anions and anion insertion. (b) Crystal field splitting of *d* orbitals by symmetry breaking.

1.2.2. Metal-insulator transitions induced by anion-doping

An increasing number of anion-doped metal oxides have been reported thanks to the establishment of effective synthesis methods. However, their transport properties are not well understood because of the lack of high-quality samples free from the influence of grain boundaries. Table 1-4 lists perovskite-related oxyhydrides and oxyfluorides whose transport properties have been investigated. Indeed, as can be seen from the Table, transport-property measurements were conducted mostly in single crystalline thin films. All the compounds in Table 1-4 except $SrCoO_{2.5}$ shows MIT by anion doping. However, the detailed mechanism of MIT has been investigated only for the upper three compounds whose crystal structures, including the positions of constituent atoms, were precisely determined by structure analysis using powder samples.

Table 1-4. Perovskite-related oxyhydrides and oxyfluorides whose transport properties have been investigated. MIT column shows whether metal-insulator transition occurs with anion doping. M, I, and SC stands for metal, insulator, and superconductor, respectively.

Product	**Precursor**	**MIT**	**Ref.**
$ATiO_{3-x}H_x$ (A = Ca, Sr, Ba)	$ATiO_3$	I to M	[20]
$Sr_2CuO_2F_{2+\delta}$	Sr_2CuO_3	I to SC	[37]
$SrVO_2H$	$SrVO_3$	M to I	[21]
$SrFeO_xH_{0.24}$ (film only)	$SrFeO_{2.5}$ / $SrFeO_2$	I to M	[23]
$NdNiO_2F$ (film only)	$NdNiO_3$	M to I	[59]
$Sr_2RuO_3F_2$ (film only)	Sr_2RuO_4	M to I	[39]
$SrCoO_xH_y$ (film only)	$SrCoO_{2.5}$	None	[24]

The insulator-to-metal transitions of ATiO$_3$ and Sr$_2$CuO$_3$ are supposed to be filling-controlled MIT (FC-MIT) induced by aliovalent anion substitution or anion insertion as described in the previous section (Figure 1-6(a)). In the case of hydride-doped ATiO$_3$, the aliovalent substitution of H^- for O^{2-} is supposed to generate one electron per H^- ($O^{2-} \rightarrow H^- + e^-$). Actually, Hall measurements revealed that the carriers in ATiO$_{3-x}$H$_x$ are electrons. Moreover, the concentrations of hydride and carrier electrons are almost the same [20], suggesting that all the emitted electrons contribute to the metallic conductivity. Sr$_2$CuO$_2$F$_{2+\delta}$ has excess fluorine atoms at the interstitial site of the layered-perovskite structure [37]. The inserted fluorine atoms generate hole carriers and the system undergoes a transition from insulator to metal and even superconducting state.

The mechanism of the metal-to-insulator transition of SrVO$_3$ was proposed, based on structure analysis and theoretical calculations [13,73], as that cooperation between electron number change (d^1 to d^2) and crystal field splitting caused MIT (Figure 1-7). The precursor SrVO$_3$ has a cubic perovskite structure in which one d-electron of V^{4+} occupies triply-degenerate t_{2g} orbitals and exhibits metallic conduction [1]. Hydride doping reduces V^{4+} (d^1) to V^{3+} (d^2). Meanwhile, *trans*-type VO$_4$H$_2$ arrangement splits t_{2g} orbitals into lower (xz, yz) and higher xy. As a result, V^{3+} in SrVO$_2$H has $(xz, yz)^{\uparrow\uparrow}$ configuration in which the electron number of each orbital is one. With this orbital occupation and Coulomb repulsion between d-electrons, SrVO$_2$H becomes a Mott insulator like Ca$_2$RuO$_4$.

The remaining three cases, SrFeO$_2$, NdNiO$_3$ and Sr$_2$RuO$_4$, are also attractive. Especially, Sr$_2$RuO$_4$ shows MIT without changing the valence state of Ru (Redox-neutral MIT) [39]. Thus, it is possible that crystal field splitting by anion doping drives the transition in this system (Figure 1-6(b)). However, it is hard to argue on the MIT

mechanisms in these compounds, mainly because of the lack of structural information; The three compounds have been obtained only in thin-film form, and, as a consequence, conventional structure-analysis methods such as Rietveld refinement cannot be used due to their small volume and large background signals from substrates.

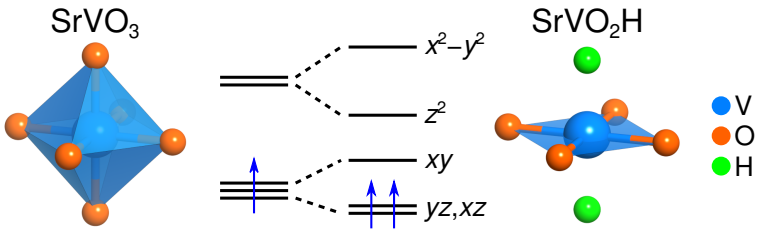

Figure 1-7. Local structures around V in $SrVO_3$ and $SrVO_2H$, and schematic diagrams for d^1 configuration in metallic $SrVO_3$ and d^2 configuration in insulating $SrVO_2H$.

1.3. Purpose of the research

Recent progress in advanced synthesis technique has opened a route to dope anionic species to metal oxides. This emerging method of chemical manipulation has widened the material variations of oxides. Among changes in physical properties caused by doping, metal-insulator transition (MIT) is one of the most outstanding and appealing phenomena. Particularly, MIT in transition metal oxides has been intensively studied so far, and several transition scenarios have been proposed such as band-width-control, filling-control, and crystal-field switching. These mechanisms seem applicable to anion-doping-driven MIT in oxides. However, experimental information, especially structural information, is insufficient to discuss MIT in some of anion-doped oxides, because they have been prepared only in thin film form.

In this thesis, I performed theoretical calculations, being complementary to experiments, to elucidate the MIT mechanism in anion-doped transition metal oxides. Recent calculation technique based on the density functional theory (DFT) enables us to predict crystal structures of solid-state materials with good accuracy. In addition, subsequent electronic-state calculations provide us valuable information to discuss the mechanisms of MIT. Indeed, DFT calculations helped us understand MIT in Sr-doped Ca_2RuO_4 and $SrVO_2H$. I theoretically investigated three compounds which lack structural information, $SrFeO_xH_{0.24}$, $NdNiO_2F$, and $Sr_2RuO_3F_2$, to determine their crystal structures and to clarify the mechanisms of MIT. This research would contribute to construction of a systematized knowledge about anion-doping induced MIT of transition metal oxides.

Chapter 2. Calculation method

All the three topics in this thesis (MIT in $SrFeO_xH_{0.24}$, $NdNiO_2F$, and $Sr_2RuO_3F_2$) have two common calculation subjects: the crystal structure of the target material, and the mechanism of the metal-insulator transition (MIT). Figure 2-1 shows how to reach these goals by theoretical calculations.

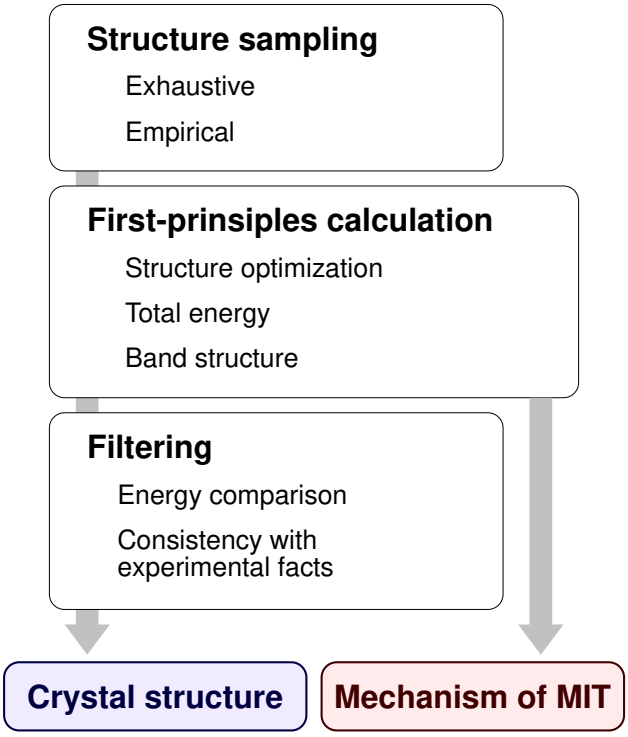

Figure 2-1. Flow chart of calculation procedure to determine crystal structures and to elucidate the mechanisms of metal-insulator transitions (MIT).

The determination of crystal structures includes three steps, as follows. The first step is listing up possible structures by an exhaustive sampling or empirical assumptions. Next, lattice constants and atomic positions of the candidates were optimized by first-principles method, and information of their internal energy and electronic structures were

also gathered. Lastly, the most likely structure was filtered out based on the collected data. In this thesis, relative energy and consistency with experimental observations (lattice constants, band gap, magnetism, and so on) were used as information for making the decision.

After the estimation of the crystal structure, the mechanism of MIT was discussed by investigating detailed electronic band structure of anion-doped materials. The most useful method is examining density of states (DOS) because it provides direct information about electronic configuration, i.e., occupation state of *d*-orbitals of transition-metal cations, which is a key to understand the mechanism of MIT as explained in 1.2.1 (p. 12). The DOS data for all the candidate structures had been already gathered in the second step of structure determination. Thus, all that is needed to do is referring to the specific data corresponding to the estimated crystal structure.

Among the three steps of the theoretical research shown in Figure 2-1, structure sampling and filtering are compound-specific. Therefore, their detailed descriptions are integrated in the chapters featuring target materials in this thesis. In this chapter, I focus on introducing basis and terminology of first-principles calculation used in the second step.

2.1. Band calculation based on the density functional theory

The main purpose of first-principles calculations in this thesis is to obtain optimized crystal structure, total energy and band structure of a given material (Figure 2-1). In this section, I introduce the basic concepts and equations which provide the necessary data.

2.1.1. Basic equations of the density functional theory [74]

Physical properties of materials are governed by quantum states of the electrons contained in the material. They travel in a potential made by atomic nuclei and all electrons except themselves. The corresponding Hamiltonian is represented as follows:

$$H = -\frac{1}{2}\sum_i \nabla_i^2 + \frac{1}{2}\sum_{i\neq j}\frac{1}{|\mathbf{r}_i - \mathbf{r}_j|} + \sum_{i,I} V_I\left(|\mathbf{r}_i - \mathbf{R}_I|\right) + E_{II} \tag{2.1}$$

Here the motion of nuclei is ignored (Born-Oppenheimer approximation). The first and second terms of the Hamiltonian are kinetic energy of electrons at $\mathbf{r}_i$ and Coulomb interaction between them, respectively. The third term denotes potential energy from nuclei at $\mathbf{R}_I$. Any approximated functions V_I can be used but the exact one is of course

$$V_I\left(|\mathbf{r}_i - \mathbf{R}_I|\right) = \frac{Z_I}{|\mathbf{r}_i - \mathbf{R}_I|} \tag{2.2}$$

The last term E_{II} includes every constant terms such as nucleus-nucleus Coulomb interaction. The Schrödinger's equation for this system is

$$H\Psi(\mathbf{r}_1, \mathbf{r}_2, \ldots) = E\Psi(\mathbf{r}_1, \mathbf{r}_2, \ldots) \tag{2.3}$$

where Ψ is the many-electron wave function. The development of the theoretical materials science is equivalent to the establishment of feasible solving procedure for the eigenvalue problem (2.3). Today's *de facto* standard method for solid-state physics is based on the

density functional theory (DFT).

The idea of DFT was proposed by Hohenberg and Kohn [75]. They proved that the many-electron wave function $\Psi(\mathbf{r}_1, \mathbf{r}_2, \ldots)$ is determined by electronic density $n(\mathbf{r})$ of the ground state. In other words, every property of a many-electron system can be expressed as functionals of electronic density $f[n(\mathbf{r})]$. This principle turned out to be a strong procedure for solving the Schrödinger's equation (2.3) after Kohn and Sham interpreted it to a handy one-electron eigenvalue problem called Kohn-Sham (KS) equation [76]:

$$H_{\mathrm{KS}}\psi_i(\mathbf{r}) = \varepsilon_i\psi_i(\mathbf{r}) \tag{2.4}$$

where $\psi_i(\mathbf{r})$ and ε_i is the one-electron wave function and the energy, respectively. The Kohn-Sham Hamiltonian H_{KS} has a typical formula in the one-electron approximation:

$$H_{\mathrm{KS}} = -\frac{1}{2}\nabla^2 + V_{\mathrm{eff}}(\mathbf{r}) \tag{2.5}$$

which expresses motion of single electron in an effective potential due to the atomic nuclei and the other electrons. The effective potential $V_{\mathrm{eff}}(\mathbf{r})$ of the KS theory consists of three terms:

$$V_{\mathrm{eff}}(\mathbf{r}) = \sum_I V_I\left(|\mathbf{r}-\mathbf{R}_I|\right) + \int \mathrm{d}^3\mathbf{r}'\frac{n(\mathbf{r}')}{|\mathbf{r}-\mathbf{r}'|} + V_{\mathrm{XC}}\left[n(\mathbf{r})\right] \tag{2.6}$$

The first term is nuclear potential and the second one is Hartree potential due to all the electrons in the system. The last $V_{\mathrm{XC}}[n(\mathbf{r})]$ is called exchange-correlation (XC) potential or XC functional which undertakes all the residual electron-electron interactions. In contrast to the many-electron systems like Equation (2.3), solving procedures for one-electron problems have already been established. The most popular one is basis expansion method:

$$\psi(\mathbf{r}) = \sum_j c_j\phi_j(\mathbf{r}) \tag{2.7}$$

where $\phi_j(\mathbf{r})$ and c_j are basis function and expansion coefficient, respectively. If we choose an orthogonal basis set, the one-electron Schrödinger's equation (2.4) comes to a matrix eigenvalue problem which can be easily implemented in computer programs:

$$\begin{pmatrix} H_{11} & H_{12} & \cdots \\ H_{21} & \ddots & \\ \vdots & & \end{pmatrix}\begin{pmatrix} c_1 \\ c_2 \\ \vdots \end{pmatrix} = \varepsilon \begin{pmatrix} c_1 \\ c_2 \\ \vdots \end{pmatrix} \qquad (2.8)$$
$$H_{ij} = \int \mathrm{d}^3\mathbf{r}\, \phi_i^*(\mathbf{r}) H_{\mathrm{KS}} \phi_j(\mathbf{r})$$

Once a set of one-electron wave functions $\{\psi_i(\mathbf{r})\}$ are obtained, the many-electron wave function of the KS system $\Psi_{\mathrm{KS}}(\mathbf{r}_1, \mathbf{r}_2, \ldots)$ can be constructed as an anti-symmetric product of $\{\psi_i(\mathbf{r})\}$. The total energy is calculated as follows:

$$\begin{aligned} E = & \frac{1}{2}\sum_i \int \mathrm{d}^3\mathbf{r} \left|\nabla \psi_i(\mathbf{r})\right|^2 \\ & + \int \mathrm{d}^3\mathbf{r} \left(\sum_I V_I\left(\left|\mathbf{r}-\mathbf{R}_I\right|\right) + \frac{1}{2}\int \mathrm{d}^3\mathbf{r}' \frac{n(\mathbf{r}')}{\left|\mathbf{r}-\mathbf{r}'\right|} + V_{\mathrm{XC}}\left[n(\mathbf{r})\right] \right) n(\mathbf{r}) + E_{II} \end{aligned} \qquad (2.9)$$

including kinetic (the first term) and potential energy (the second term) of electrons, and the constant nucleus-nucleus interaction energy (the third term).

2.1.2. Application to the band theory for solid-state systems

The KS equation (2.4) and solving technique using basis expansion (2.7) can be easily applied to the band theory for periodic solid-state systems. The corresponding KS equation is

$$\left[-\frac{1}{2}\nabla^2 + V_{\mathrm{eff}}(\mathbf{r}) \right] \psi_{\mathbf{k}n}(\mathbf{r}) = \varepsilon_{\mathbf{k}n} \psi_{\mathbf{k}n}(\mathbf{r}) \qquad (2.10)$$

where the one-electron wave functions $\psi_{\mathbf{k}n}(\mathbf{r})$ are equivalent to the Bloch waves in the band theory indexed with wave vector $\mathbf{k}$ and band number n. A set of the one-electron

energy $\varepsilon_{\mathbf{k}n}$ provides information of band structure. Particularly, density of states (DOS) is equivalent to histogram of $\varepsilon_{\mathbf{k}n}$. The total energy is calculated in the same manner as Equation (2.9) but the sum operation over i is replaced by a weighted summation of n and integration of $\mathbf{k}$ over the Brillouin zone (BZ):

$$\sum_i \rightarrow \sum_n \int_{\mathrm{BZ}} \mathrm{d}^3\mathbf{k}\, f_{\mathbf{k}n} \tag{2.11}$$

where the weight factor $f_{\mathbf{k}n}$ is occupation number (0–1) of the corresponding Bloch state $\psi_{\mathbf{k}n}$. Structure optimization is performed by iteration of the two following steps. The first step is evaluation of forces on nuclei $\mathbf{F}_I$ by energy derivative with respect to nuclear position $\mathbf{R}_I$:

$$\mathbf{F}_I = -\frac{\partial E}{\partial \mathbf{R}_I} \tag{2.12}$$

Then, all the positions $\{\mathbf{R}_I\}$ are displaced towards $\{\mathbf{F}_I\}$ so that residual forces get smaller.

In summary, all the necessary information in this study can be derived from the KS equation (2.10). To perform actual calculations, it is needed to specify all the items included in the KS theory. In the next section, I explain the detailed implementation of the items listed below of which detailed formulation has not been mentioned yet.

Item	
XC functional	$V_{\mathrm{XC}}[n(\mathbf{r})]$
Basis set	$\{\phi_j(\mathbf{r})\}$
Electron-nucleus potential	$V_I(r)$
BZ integration method	$\int_{\mathrm{BZ}} \mathrm{d}^3\mathbf{k}$

2.2. Detailed implementations

2.2.1. Exchange-correlation (XC) functional [74]

A critical problem of the KS approach is that the exact formulation of the XC functional $V_{XC}[n(\mathbf{r})]$ is unknown while its existence is guaranteed by Hohenberg-Kohn principles of DFT. Therefore, actual calculations have been performed using approximated XC functionals. So far, various flavors of $V_{XC}[n(\mathbf{r})]$ have been proposed and some of them are employed in today's DFT calculations. The simplest and earliest approach is local density approximation (LDA). LDA is based on an idea for applying V_{XC} of homogenous electrons to general systems. While LDA functional works well for itinerate electron systems such as metals, it has large error for materials with steep change of electronic density. Accordingly, the generalized gradient approximation (GGA) was developed. In GGA approach, XC potential is constructed as a functional of not only electronic density but also gradient of it: $V_{XC}[n(\mathbf{r}), \nabla n(\mathbf{r})]$.

Now GGA functional is a standard choice for band calculation based on DFT. Especially, implementation by Perdew, Burke, and Ernzerhof (PBE) [77] is widely used. Meanwhile, it often fails for compounds including transition metal elements. For example, GGA functionals severely underestimate the band gaps of insulating transition-metal oxides or even give wrong metallic states. The major source of the error is Hartree term of KS effective potential $V_{eff}(\mathbf{r})$ (Eq. (2.6))

$$\int d^3\mathbf{r}' \frac{n(\mathbf{r}')}{|\mathbf{r}-\mathbf{r}'|} \tag{2.13}$$

which includes unphysical interaction of electron with itself. It spuriously overestimates the energy levels ε_i of occupied orbitals and results in underestimation of the band gap.

This fault of KS effective potential, called self-interaction error (SIE), is significant for transition metal compounds with localized *d* and *f* electrons. Thus, most theoretical studies on transition metal compounds have utilized modified GGA functionals. Especially, hybrid functional and GGA + *U* method are intensively adopted in these days.

Hybrid functional comes from an idea for supplementing GGA with Hartree-Fock approximation (HFA). While HFA is also a one-electron approximation using effective potential $V_{\mathrm{eff}}(\mathbf{r})$, it is fundamentally free from SIE because the Fock exchange term in V_{eff} completely offsets the self-interaction included in the Hartree term. Accordingly, hybrid functional incorporates the Fock exchange term into GGA functional:

$$V_{\mathrm{XC}}^{\mathrm{Hybrid}} = V_{\mathrm{XC}}^{\mathrm{GGA}} + C\left(V_{\mathrm{X}}^{\mathrm{HF}} - V_{\mathrm{X}}^{\mathrm{GGA}}\right) \tag{2.14}$$

where Fock exchange $V_{\mathrm{X}}^{\mathrm{HF}}$ is added with a mixing ratio *C*, and double counting of exchange interaction by GGA and HF is corrected by subtracting GGA exchange $V_{\mathrm{X}}^{\mathrm{GGA}}$. Practically, $V_{\mathrm{X}}^{\mathrm{HF}}$ is difficult to calculate for infinite periodic systems because of the long-range nature of Coulomb interaction. One solution for this difficulty was proposed by Heyd, Scuseria, and Ernzerhof [78]. They divided the Coulomb potential into short-range and long-range terms by the error function with a screening parameter μ:

$$\frac{1}{r} = \frac{1-\mathrm{erf}\left(\mu r\right)}{r} + \frac{\mathrm{erf}\left(\mu r\right)}{r} \tag{2.15}$$

and calculated the Fock exchange only for the short-range (SR) term. The calculated SR $V_{\mathrm{X}}^{\mathrm{HF}}$ is incorporated into PBE functional with a mixing parameter of 1/4.

$$V_{\mathrm{XC}}^{\mathrm{HSE}} = V_{\mathrm{XC}}^{\mathrm{PBE}} + \frac{1}{4}\left(V_{\mathrm{X,SR}}^{\mathrm{HF}} - V_{\mathrm{X,SR}}^{\mathrm{PBE}}\right) \tag{2.16}$$

This XC functional, called HSE functional, was found to drastically improve the accuracy of calculation for transition-metal compounds.

One problem of HSE functional is its calculation time. Because calculation of Fock

exchange term needs highly-nested iteration, HSE calculation takes much longer time than GGA calculation. Therefore, another type of modified GGA, called GGA + *U* method [79], is also intensively used. It incorporates the Coulomb repulsion *U* of the Hubbard model with GGA functional. This extension improves the band positions of *d* and *f* electrons with only slight increase of calculation time. In actual calculations, we need to specify the *U* value for each *d* or *f* orbital of transition-metal element. Usually, the *U* values are empirically chosen so that experimental observations are reproduced. Meanwhile, a simple method to theoretically determine optimal *U* values has been proposed by Cococcioni *et al.* [80]. Their strategy can be derived by reviewing the GGA + *U* correction using an isolated atomic system (Figure 2-2) which is an extreme case with localized electrons. In this system, the exact total energy with respect to the continuous number of electrons can be expressed as a linear combination of the energy with the neighboring integer electrons:

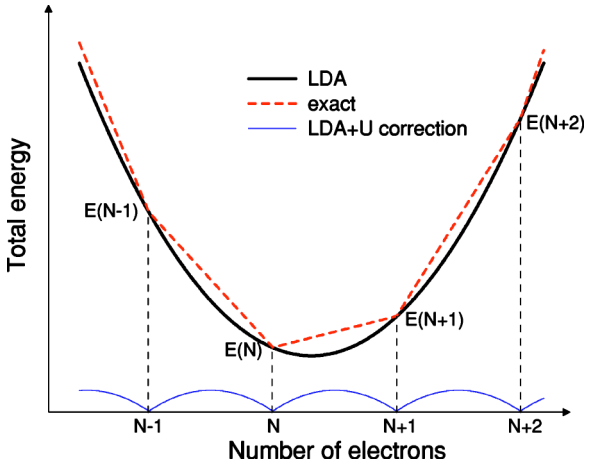

Figure 2-2. Schematic image of the total energy of an isolated atomic system in contact with a electron reservoir. The black and red lines depict results with the LDA and the exact formulation, respectively. The blue line is the difference between them to be corrected by the LDA/GGA + *U* method. Reprinted with permission from Ref. [80]. Copyright 2005 by the American Physical Society.

$$E_{N+\omega} = (1-\omega) E_N + \omega E_{N+1} \tag{2.17}$$

where N is a positive integer and ω is any fraction from 0 to 1. Therefore, $E_{N+\omega}$ becomes lowest with a certain integer number of electrons (the red line in Figure 2-2). On the other hand, total energy calculations based on the LDA and GGA give unphysical curvatures mainly due to the SIE, and the optimal electron number is often not an integer (the black line in Figure 2-2). This is another representation of the failure of the LDA and GGA giving wrong metallic states (fractional occupation) for insulating systems (integer occupation) of *d* or *f* electrons. The GGA + U method remedies this undesirable behavior by adding a quadratic correction term with respect to occupation numbers of the sites:

$$E_U = \frac{U}{2} \sum_i n_i (1-n_i) \tag{2.18}$$

where n_i is the electron number in the orbitals of interest i ($0 \leq n_i \leq 1$). E_U destabilize fractional occupation and thus make systems more likely to be insulator. The optimal U values should be chosen so that the quadratic correction E_U restores the exact energy profile for the localized electron system (blue line in Figure 2-2). Therefore, U can be estimated from the curvature (second order derivative) of the GGA energy with respect to occupation numbers n_i:

$$U = \frac{\partial^2 E}{\partial^2 n_i} = \frac{\partial \varepsilon_i}{\partial n_i} \tag{2.19}$$

where Janak theorem [81] is used to convert the second order derivative of the total energy to the first order derivative of the one-electron energy of the orbital ε_i. The final expression by Cococcioni *et al.* is derived by a Legendre transform and substituting derivative of ε which can be more easily implemented than the derivative of n:

$$U = \chi_{\mathrm{nsc}}^{-1} - \chi_{\mathrm{sc}}^{-1}, \quad \chi = \frac{\partial n}{\partial \varepsilon} \tag{2.20}$$

In this method, the energy level of the orbital of interest is artificially shifted by $\partial\varepsilon$, and the response of the occupation number of that orbital ∂n is examined. The differential coefficient χ is calculated under two conditions: non-self-consistent (nsc) and self-consistent (sc). To calculate χ_{nsc}, the charge density of the ground state ($\alpha = 0$) was used as a fixed parameter, while the charge density in the χ_{sc} calculation was updated with respect to the applied potential $\partial\varepsilon$. The purpose of calculating χ_{ncs} is to evaluate the excess curvature originating from a rehybridization with noninteracting bands. After both differential coefficients are obtained, the optimal U value is given as difference of reciprocals.

2.2.2. Basis set

In the band theory, Bloch theorem is derived by expressing wave functions in periodic potential using plane waves. Therefore, it is reasonable to use them as a basis set for actual band calculations. Bloch waves are expanded by plane waves as follows:

$$\psi_{\mathbf{k}n}(\mathbf{r}) = \frac{1}{\sqrt{V}} \sum_{\mathbf{G}} c_{\mathbf{k}n,\mathbf{G}} e^{i(\mathbf{G}+\mathbf{k})\cdot\mathbf{r}} \tag{2.21}$$

where V is the volume and $\mathbf{G}$ is the reciprocal lattice points. The size of basis is specified by cutoff energy E_{cutoff}. All the plane waves whose energy is not larger than the cutoff are included:

$$\frac{1}{2}\left|\mathbf{G}+\mathbf{k}\right|^2 \leq E_{\mathrm{cutoff}} \tag{2.22}$$

Equation (2.22) also suggests that the cutoff energy is equivalent to the spatial resolution of the basis set. If a material of interest is expected to have an electronic density distribution with a steep gradient, one needs to use a plane-wave basis set with high

energy cutoff.

2.2.3. Electron-nucleus potential

The valence orbitals calculated with the exact nucleus potential (Eq. (2.2)) have dense nodes near nuclei due to the orthogonality of orbitals. They require a large plane-wave basis set as mentioned above. Therefore, approximated nuclei potential $V_I(\mathbf{r})$, called pseudopotential, is used in band calculation with plane-wave basis set. In this method, inner core electrons are incorporated in the potential of nuclei. As a result, approximated valence wave functions are free from nodes near the nuclei and they can be described by a reasonable size of plane-wave basis set. Several kinds of pseudopotential have been proposed. Especially, the projector augmented wave (PAW) method using information of inner electrons is more accurate than other methods [82].

2.2.4. Brillouin zone integration

In actual calculation, the integration with respect to wave vector **k** over the Brillouin zone is approximated by numerical summation over a finite number of **k** points.

$$\int_{\mathrm{BZ}} \mathrm{d}^3\mathbf{k} \quad \rightarrow \quad \frac{1}{N_{\mathbf{k}}} \sum_{\mathbf{k}} \tag{2.23}$$

Monkhorst and Pack found that a uniform sampling along reciprocal lattice vector suffices for practical use [83]. In this method, a set of **k** points are generated as follows:

$$\mathbf{k} = \frac{n_1}{N_1}\mathbf{b}_1 + \frac{n_2}{N_2}\mathbf{b}_2 + \frac{n_3}{N_3}\mathbf{b}_3, \quad \left(n_i = 0 \ldots N_i\right) \tag{2.24}$$

where $\mathbf{b}_i$ are reciprocal vectors.

2.3. Methods employed in this thesis

In this thesis, structure optimization, total energy and electronic state calculation were performed by band calculation based on the density functional theory implemented in Vienna ab initio simulation package (VASP) software [84]. For the exchange-correlation functional in Kohn-Sham equation, I used HSE functional [78] and GGA + U [79,85] method because all the calculation targets in this thesis are transition metal compounds and researches of metal-insulator transition require high accuracy for their electronic band structures. The U values for transition metal elements were determined so that experimental observations such as lattice constants and band gaps were reproduced. In case of $Sr_2RuO_3F_2$, I used the first-principles method proposed by Cococcioni *et al* [80]. to evaluate the optimal U value for Ru 4*d* orbital. The valence Bloch wave functions were described by a plane-wave basis set. The other core electrons were taken into account by the projector augmented wave (PAW) method [82,86]. Brillouin zone integration was carried out by the Monkhorst-Pack scheme [83].

Chapter 3. Insulator-to-metal transition of $SrFeO_2$ by hydrogen doping[†]

3.1. Introduction

The recent development of topochemical reactions using solid-state reductants, such as CaH_2 and NaH, at modestly high temperatures of $200 < T < 600$ °C has presented methods to introduce large amounts of oxygen vacancies or hydrogen into transition-metal oxides without changing their cation frameworks [87]. This reaction method has provided us with a new research field involving the modification of the physical properties of existing transition-metal oxides.

In particular, the effect of hydrogenation has been discussed for a series of transition metal oxides with perovskite-type structures [9–14,17,20,22]. In these compounds, the hydrogen atoms were characterized as hydrides at lattice oxygen sites (H_O^-) by X-ray/neutron Rietveld refinements or thermal gravimetric analysis. In the titanium oxides $ATiO_{3-x}H_x$ (where A = Ca, Sr, Ba, or Eu), the H_O^- doping generates one free electron per H atom ($O^{2-} \rightarrow H_O^- + e^-$) and causes insulator-to-metal transitions [10–12,20,88]. The incorporation of hydride into O-sites can also induce antiferromagnetic

[†] This chapter contains the contents of the following publication.

"First-Principles Calculations on the Crystal/Electronic Structure and Phase Stability of H-Doped $SrFeO_2$"
Yuji Kurauchi, Hideyuki Kamisaka, Tsukasa Katayama, Akira Chikamatsu, and Tetsuya Hasegawa
J. Phys. Chem. C **121**, 7478 (2017).

(AFM) orderings of *B*-site cation spins at high Néel temperatures of T_N > 300 K, as seen in $SrCrO_2H$ and $Sr_2CoO_3H_{0.7}$ [9,17]. The AFM state of $Sr_2CoO_3H_{0.7}$ is due to the strong σ-bonding of Co(e_g)–H(1*s*)–Co(e_g) [9,89], whereas the stability of the AFM state in $SrCrO_2H$ is suggested to come from the original Cr(t_{2g})–O(2*p*) π-type interaction enhanced by the hydride substitution [90].

Reactions with solid-state reductants can also modify the structures of transition metal oxides through the introduction of a large amount of oxygen vacancies [87]. A typical example is the synthesis of $SrFeO_2$ by reacting the precursor $SrFeO_{3-\delta}$ with CaH_2 [91]. $SrFeO_2$ has a so-called infinite-layer structure (space group: *P*4/*mmm*) with corner-sharing FeO_2 square nets separated by Sr ions (Figure 3-1), and bulk $SrFeO_2$ is reported to be an AFM insulator with a Néel temperature of 473 K [91]. On the other hand, Katayama *et al*. performed a similar CaH_2 treatment of $SrFeO_{3-x}$ thin films and found that the obtained film contains 0.24 hydrogen atoms per formula unit (4×10^{21} cm^{-3}), possibly due to the more efficient diffusion of hydrogen [23]. The $SrFeO_xH_{0.24}$ (SFOH) film exhibited metallic conduction, suggesting carrier doping by H_O^- or H^+ inserted between FeO_2 sheets. However, the microscopic location of the hydrogen atoms is unknown because neither Rietveld refinements nor thermal gravimetric analyses are applicable to thin films due to their small volume and the relatively large background signals from substrates. Furthermore, the carrier electron density per hydrogen is as low as ~0.1% (3.1×10^{18} cm^{-3}) [23], suggesting the presence of electron trapping states.

In this study, I conducted first-principles density functional theory (DFT) calculations to investigate the crystal and electronic structures of SFOH, and analyzed its phase stability based on thermodynamic analysis. The results indicated the incorporation of hydride anions, and led us to conclude that SFOH consists of an insulating matrix and

metallic domains.

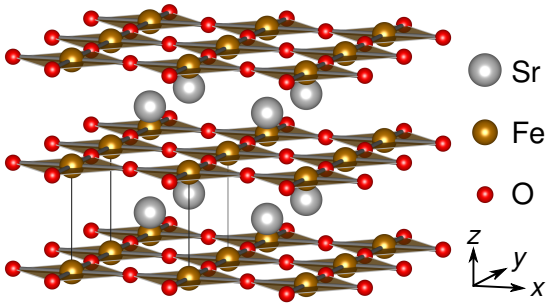

Figure 3-1. Crystal structure of $SrFeO_2$. Solid lines enclose a primitive cell.

3.2. Calculation method

All of the present calculations were performed for periodic model unit cells using a plane-wave basis set as implemented in the VASP software package [84]. For the DFT functional, the hybrid functional proposed by Heyd–Scuseria–Ernzerhof (HSE) was adopted with the range separation parameter $\mu = 0.2$ Å^{-1} (HSE06) [78]. The effect of core electrons was incorporated using the projector augmented wave approach (PAW) [82,86]. The cutoff energy was 600 eV for valence electronic states, composed of $4s^2 4p^6 5s^2$ electrons in Sr, $3p^6 3d^6 4s^2$ in Fe, $2s^2 2p^4$ of O, and $1s^1$ in H. The Brillouin zone integration was carried out according to the Monkhorst–Pack k-point scheme [83], with the density of the mesh point being ca. 5000 points Å^3. It was assumed that the SFOH maintains the G-type **q** = (1/2, 1/2, 1/2) antiferromagnetic order [91], and thus used the spin-polarized method. Auxiliary utilities, Bader charge analysis [92] and VESTA [4] were used for population analysis of the valence electrons and visualization of the crystal structures, respectively.

It is worth discussing the choice of the HSE functional. Reliable prediction of electron trapping/conducting character requires a careful choice of DFT functional.

Conventional semilocal functionals tend not to reproduce the electron trapping states well because of their self-interaction error (SIE). This error results in the spurious repulsion of an electron by itself, resulting in unphysical delocalization of the electrons. In the hybrid functional, the problem of SIE is remedied by inclusion of the exact exchange term, as in the case of the Hartree–Fock approximation.

The calculation with the HSE functional well reproduced the lattice constants of pristine $SrFeO_2$, and the electronic structure reported in literature using the GGA+U method (Figure 3-2) [93,94]. Optimized lattice constants were a = 3.998 Å and c = 3.470 Å, which are in good agreement with the experimental values: a = 3.985 Å and c = 3.458 Å at 10 K [91]. The HSE functional successfully described the divalent (d^6) iron with an anomalous high-spin ($S = 2$) state having one minority-spin electron in the d_z^2 orbital. The order of d-bands was also consistent with that reported in the previous works using the GGA+U method.

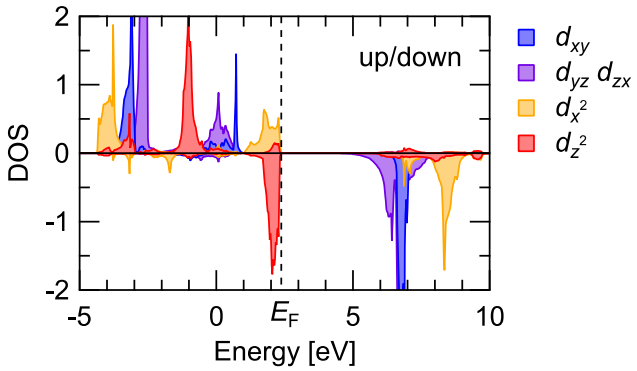

Figure 3-2. Partial density of states (PDOS) for 3d electrons of Fe in pristine $SrFeO_2$. A vertical broken line denotes the position of the Fermi energy. The x, y, and z coordinates are the same as those in Figure 3-1.

Determination of the optimal locations and chemical states of the hydrogen atoms was carried out for a 2 × 2 × 2 super cell of the primitive $SrFeO_2$ unit. Two hydrogen

atoms were added to the cell, giving a theoretical hydrogen concentration of 0.25 per formula unit (f.u.$^{-1}$), which is close to the experimental value of 0.24 f.u.$^{-1}$ [23]. It was assumed that the hydrogen atoms are either positioned at interstitial sites (H_i) or substitute lattice oxygen atoms (H_O). Three combinations of H_i and H_O were considered for these two hydrogen atoms: two interstitial sites ([$2H_i$]), two oxygen sites ([$2H_O$]), and their combination ([H_iH_O]). For each combination, relative spatial orientations of the two hydrogen atoms were varied. Ionic positions and lattice constants were optimized for all considered unit cells until the largest residual force on an atom and the pressure on the cell became < 0.01 eV Å^{-1} and < 0.1 GPa, respectively.

3.3. Results and discussion

Figure 3-3 shows the crystal structures with the two lowest total energy values for the three anion compositions [$2H_i$], [H_iH_O], and [$2H_O$], where [X]^{first} and [X]^{second} denote the structures with the lowest and the second lowest total energy, respectively. As seen from the figure, interstitial hydrogen atoms H_i prefer to be located at the apical sites that were originally occupied by oxygen in the initial perovskite structure rather than to make O–H_i hydroxide bonds. Except for the [H_iH_O] group, the hydrogen atoms are aligned in a 1D manner with little distortion of the FeO_2 square network in the stable structures.

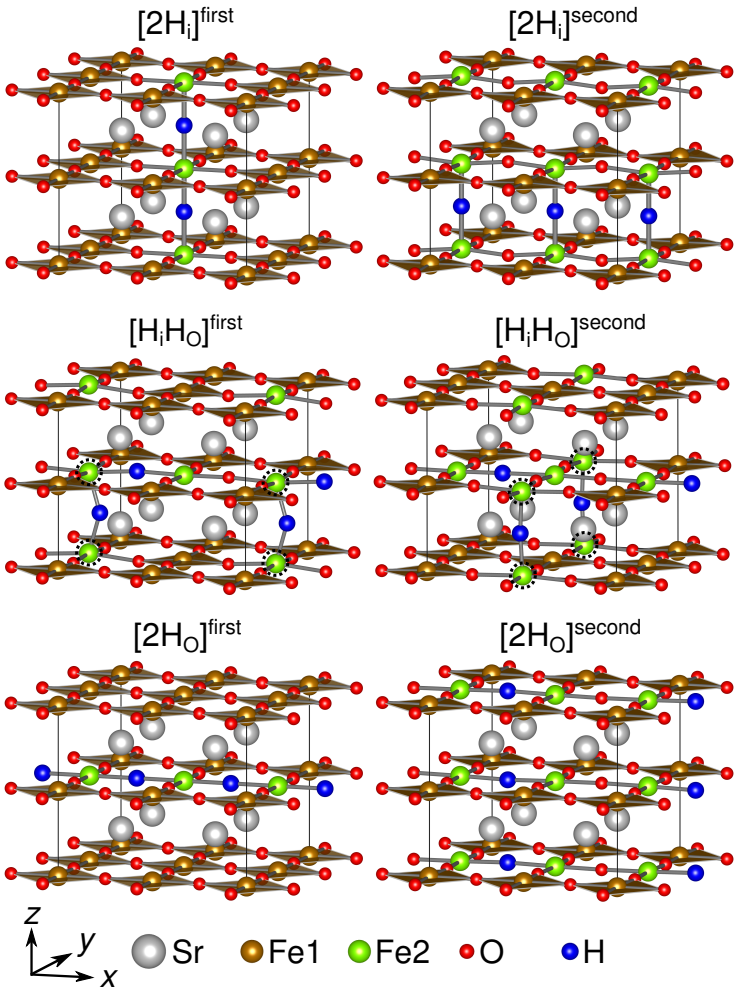

Figure 3-3. Crystal structures with the lowest total energy values. Fe atoms are distinguished by whether they are adjacent to H (green) or not (orange). In the $[H_iH_O]$ structures, Fe2 atoms with apical hydrogen are surrounded by broken circles.

Table 3-1 summarizes characteristics of the structures shown in Figure 3-3 and undoped $SrFeO_2$ for comparison. The atomic charge states and the magnetic moment values of Fe and H were evaluated by Bader charge analysis [92] and summation of spin polarization in PAW spheres, respectively. The Bader charge and magnetic moment of high-spin Fe^{2+} in undoped $SrFeO_2$ were estimated to be +1.27 *e* and 3.62 μ_B, respectively. Compared with its nominal values, +2 *e* and 4 μ_B, the calculated values are generally underestimated due to spread of electronic population. The charge and magnetic moment

Table 3-1. Average Bader charge and magnetic moment of Fe/H and Fe–O/Fe–H bond length in the structures in Figure 3-3 and Undoped $SrFeO_2$.

cell	bader charge (e)	magnetic moment (μ_B)	bond length (Å)	cell	bader charge (e)	magnetic moment (μ_B)	bond length (Å)
Undoped							
Fe	+1.27	3.62					
Fe–O			2.00				
$[2H_i]^{first}$				**$[2H_i]^{second}$**			
Fe1	+1.21	3.61		Fe1	+1.27	3.62	
Fe2	+1.66	3.94		Fe2	+1.47	3.71	
H_i	−0.56	0.00		H_i	−0.49	0.00	
Fe1–O			1.99	Fe1–O			1.99
Fe2–O			2.00	Fe2–O			2.01
Fe2–H_i			1.76	Fe2–H_i			1.72
$[H_iH_O]^{first}$				**$[H_iH_O]^{second}$**			
Fe1	+1.25	3.62		Fe1	+1.23	3.59	
Fe2	+1.21	3.55		Fe2	+1.23	3.59	
H_i	−0.55	0.00		H_i	−0.53	0.00	
H_O	−0.63	0.00		H_O	−0.63	0.00	
Fe1–O			2.00	Fe1–O			2.00
Fe2–O			2.00	Fe2–O			2.00
Fe2–H_i			1.74	Fe2–H_i			1.72
Fe2–H_O			2.06	Fe2–H_O			2.07
$[2H_O]^{first}$				**$[2H_O]^{second}$**			
Fe1	+1.24	3.62		Fe1	+1.20	3.63	
Fe2	+0.67	3.10		Fe2	+0.99	3.40	
H_O	−0.66	0.00		H_O	−0.64	0.00	
Fe1–O			2.00	Fe1–O			2.00
Fe2–O			1.93	Fe2–O			1.96
Fe2–H_O			2.00	Fe2–H_O			2.02

of Fe in the H-doped systems depend on its position. The Fe atoms not adjacent to hydrogen (Fe1 in Figure 3-3) have almost the same charge and magnetic moment values as those in undoped $SrFeO_2$. On the contrary, the values of Fe adjacent to hydrogen (Fe2 in Figure 3-3) differ between [$2H_i$], [H_iH_O], and [$2H_O$] structures, implying changes in valence states and *d* electron configurations caused by the neighboring hydrogen. The Bader charges of hydrogen are in the range of −0.49 *e* to −0.56 *e* for H_i atoms and −0.63 *e* to −0.66 *e* for H_O atoms. Those in CaH_2 and H_2O as references were evaluated to be −0.72 *e* and +1.00 *e*, respectively, and thus it can be concluded that the hydrogen in $SrFeO_2$ exists as hydride (H^-).

The electron population analysis (Table 3-1) suggested changes in the valence state and *d* electron configurations in Fe adjacent to hydrogen (Fe2 in Figure 3-3). The chemical formulae of the [$2H_i$] and [$2H_O$] structures are $SrFeO_2H^-_{0.25}$ and $SrFeO_{1.75}H^-_{0.25}$, respectively. According to the limitation of valence neutrality, the iron in the [$2H_i$] and [$2H_O$] cells should be oxidized and reduced, respectively, from the divalent Fe^{2+}. I assessed the valence state of iron by calculating the partial density of states (PDOS) for Fe-3*d* electrons. Because the 3*d* bands are well localized, PDOS is useful to determine the electron occupations of the states and estimate the nominal charges of atoms more clearly than with Bader's analysis. Figure 3-4 shows the PDOS for minority-spin d_{zx} and d_{z^2} components of Fe2 along with the PDOS for H-1*s* electrons. Because the *d*-electron configuration of high-spin Fe^{2+} (d^6) ions in the pristine $SrFeO_2$ is $(xy)^{\uparrow}(yz, zx)^{\uparrow\uparrow}(x^2-y^2)^{\uparrow}(z^2)^{\uparrow\downarrow}$ [93,94], the minority-spin d_{yz}/d_{zx}-band is empty and the d_{z^2}-band is occupied (Figure 3-4(a)). All iron atoms not adjacent to a hydrogen (Fe1 in Figure 3-3) are in a similar divalent state, which is consistent with the results of population analysis in Table 3-1. Conversely, the electronic state of iron adjacent to the hydrogen atoms (Fe2

in Figure 3-3) in [2H_i] and [2H_O] deviates from the divalent state. The d_z^2-band of Fe2 in the [2H_i] cells releases its electron and becomes partially filled (nominally $Fe^{2.5+}$) in $[2H_i]^{second}$, or even empty (Fe^{3+}) in $[2H_i]^{first}$ (Figure 3-4(b,c)). In contrast, the d_{zx}-band in the [2H_O] cells accommodates an additional electron, and the band becomes partially filled ($Fe^{1.5+}$) in $[2H_O]^{second}$ or totally filled (Fe^{+}) in $[2H_O]^{first}$ (Figure 3-4(d,e)). It should be noted that the degeneracy of the d_{yz} and d_{zx} orbitals in undoped $SrFeO_2$ is broken in Fe2 atoms in the [2H_O] structures because of different bond lengths between Fe2–O and Fe2–H_O (Table 3-1). Only the d_{zx} orbital accommodates electrons whose lobe is directed along the Fe2–H_O bond (Figure 3-3) and thus receives relatively smaller Coulomb repulsion from O-2*p* electrons in the atom. The nominal magnetic moment on Fe2 for all respective cases can be estimated as 5 μ_B (Fe^{3+}), 4.5 μ_B ($Fe^{2.5+}$), 3.5 μ_B ($Fe^{1.5+}$), and 3 μ_B (Fe^{+}). Table 3-1 confirms that the decrease of Bader charges and magnetic moments of Fe2 in [2H_O] and [2H_i] structures is in this order. In conclusion, oxidation or reduction of iron occurs only for the nearest neighbors to the hydrogen, and the charge state of iron depends on the configurations of the hydrogen atoms.

The PDOS of H-1*s* electrons spreads over the valence band and a few states in the conduction band (Figure 3-4), which supports the conclusion based on the Bader charge analysis (Table 3-1) that the chemical state of hydrogen is hydride. The distribution of H-1*s* states in the [2H_i] structures is similar to that of Fe-3d_z^2 (Figure 3-4(b,c)), which indicates hybridization between them. This hybridization originates from orbital overlap in the Fe2–H_i bond along the *z* axis (Figure 3-3). In contrast, PDOSs of H_i-1*s* and d_{zx} in [2H_i] (Figure 3-4(b,c)), and those of H_O-1*s* and the *d* orbitals in [2H_O] (Figure 3-4(d,e)) are not correlated, reflecting their negligibly weak interactions.

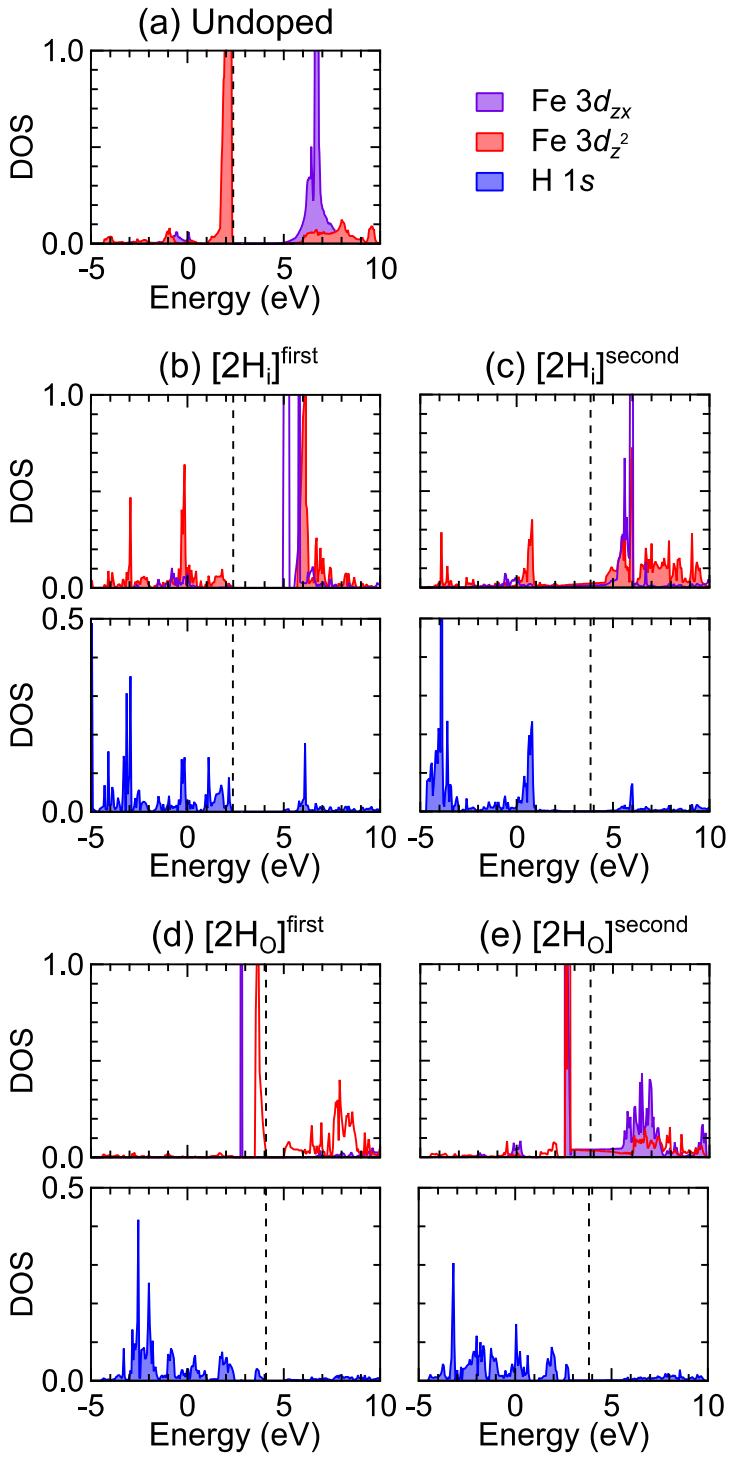

Figure 3-4. PDOS for minority-spin d_{zx} and d_z^2 electrons of iron and 1s electrons of hydrogen atoms. (a) Undoped $SrFeO_2$. (b,c) Fe2 and H in $[2H_i]^{first}$ and $[2H_i]^{second}$. (d,e) Fe2 and H in $[2H_O]^{first}$ and $[2H_O]^{second}$. Vertical broken lines denote the Fermi energy. The x, y, and z coordinates are the same as those in Figure 3-3.

The electron occupation in the d_{zx} and d_z^2 band governs the electronic conduction properties of [$2H_i$] and [$2H_O$]. Figure 3-5(a,b) and Figure 3-5(e,f) show the total DOS for the $[2H_i]^{first/second}$ and $[2H_O]^{first/second}$ structures, respectively. Model cells with the partially filled *d*-band, $[2H_i]^{second}$ and $[2H_O]^{second}$, show "metallic" DOS with finite density of states at the Fermi energy (E_F) (Figure 3-5(b,f)). Meanwhile, other models with integer occupation numbers, $[2H_i]^{first}$ and $[2H_O]^{first}$, exhibit an insulating feature characterized by a gap at E_F (Figure 3-5(a,e)).

All of the iron ions in [H_iH_O] are divalent, as expected from the composition $SrFeO_{1.875}H^-_{0.25}$. However, the *d*-electron configuration of Fe2 with apical hydride (surrounded by broken circles in Figure 3-3) is different from that in pristine $SrFeO_2$; the minority spin occupied not the d_z^2 orbital but the d_{zx} orbital. Because the fully occupied 1*s* orbital of the apical hydride has a large overlap with the d_z^2 orbital immediately below, the occupation of d_z^2 should be suppressed by Coulomb repulsion. Figure 3-5(c,d) shows the total DOSs for $[H_iH_O]^{first}$ and $[H_iH_O]^{second}$, respectively. The band of the destabilized d_z^2 orbital is located in the conduction band in the total DOS. In case of $[H_iH_O]^{second}$, however, the bottom of the d_z^2 band traverses the Fermi energy, resulting in the metallic DOS (Figure 3-5d).

Table 3-2 summarizes the nominal charge state of iron in each model and indicates whether the compound is metallic or insulating. Because the incorporated hydrogen affects the charge state of adjacent iron atoms, the over-all electronic band structure is sensitive to the hydrogen configuration.

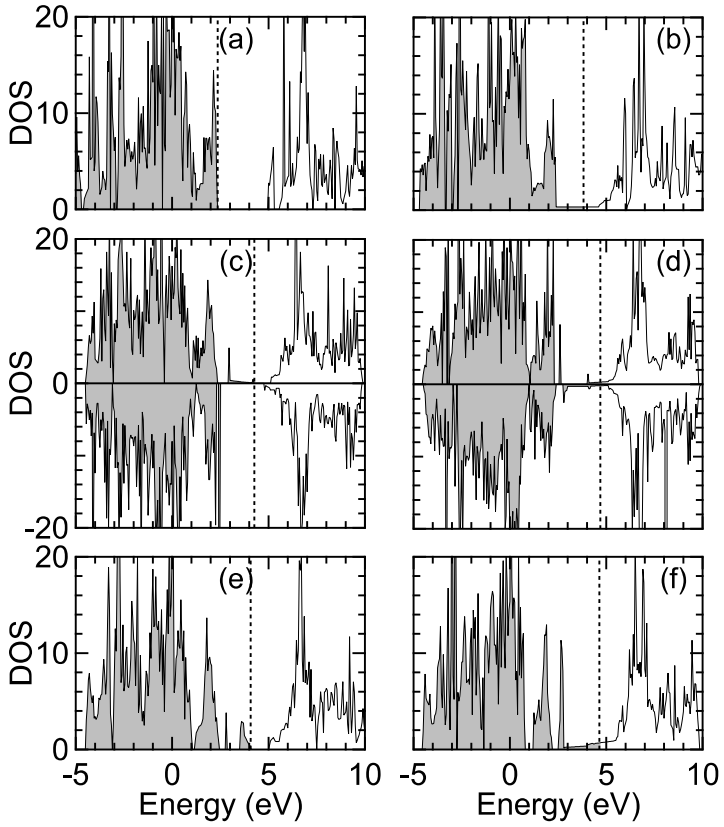

Figure 3-5. Total DOS for the structures in Figure 3-3. (a) $[2H_i]^{first}$. (b) $[2H_i]^{second}$. (c) $[H_iH_O]^{first}$. (d) $[H_iH_O]^{second}$. (e) $[2H_O]^{first}$. (f) $[2H_O]^{second}$. $[2H_i]$ and $[2H_O]$ have symmetric DOS with respect to spins, and thus only one spin direction is depicted. Vertical broken lines denote the Fermi energy.

Table 3-2. Nominal charge states of iron and conductivities of the structures shown in Figure 3-3.

cell	charge states of Fe	conductivity
$[2H_i]^{first}$	Fe^{2+} 75% : Fe^{3+} 25%	insulator
$[2H_i]^{second}$	Fe^{2+} 50% : $Fe^{2.5+}$ 50%	metal
$[H_iH_O]^{first}$	Fe^{2+}	insulator
$[H_iH_O]^{second}$	Fe^{2+}	metal
$[2H_O]^{first}$	Fe^{2+} 75% : Fe^{+} 25%	insulator
$[2H_O]^{second}$	Fe^{2+} 50 % : $Fe^{1.5+}$ 50 %	metal

Next, I examined the phase stability of SFOH by comparing the change in the Gibbs free energy, $\Delta G = G_{\text{product}} - G_{\text{reactant}}$, associated with the reactions forming SFOH from $SrFeO_{2.5}$ and CaH_2, as illustrated in Figure 3-6. The ΔG value for undoped $SrFeO_2$ is also presented for comparison. Although the details of the H-doping process with CaH_2 are still a matter of debate, the formation of CaO and H_2 species as its byproduct has been suggested in several reports [95,96]. I employed the following reaction formula:

$$\mathrm{SrFeO_{2.5}} + 0.75\mathrm{CaH_2} \rightarrow \mathrm{SrFeO_{2-\delta}H_{0.25}} + (0.5+\delta)\mathrm{CaO} + (0.375+\delta)\mathrm{H_2} + (0.25-\delta)\mathrm{CaH_2}$$

where the change of the Gibbs energy is denoted as $\Delta G[X]$ (X = $2H_i$, $2H_O$, H_iH_O, or undoped). The free energy of each species was estimated using the total energy obtained by DFT calculation. Lattice vibrations were not included in the present analysis because their contributions to ΔG are anticipated to be negligibly small. The free energy of the produced H_2 gas was evaluated by counting both its translational and rotational motions at T = 520 K. The partial pressure of the emitted H_2 gas (P_{H2}) was assumed to be from 1 Pa to 10^4 Pa. The hydrogenation reaction was performed using a sealed glass tube containing large excess CaH_2. Under this circumstance, oxygen molecules immediately react with CaH_2 and will be eliminated from the system. Therefore, the partial pressure of O_2 gas was regarded as zero.

Figure 3-7 shows the calculated $\Delta G[X]$ as a function of P_{H2}, where the solid and dashed lines in the figure represent $\Delta G[X]^{\text{first}}$ and $\Delta G[X]^{\text{second}}$, respectively. Notably, $\Delta G[2H_O]^{\text{first}}$ (blue solid line) is the lowest under H_2 pressures up to 10^4 Pa, followed by the second group, $\Delta G[2H_O]^{\text{second}}$, $\Delta G[H_iH_O]^{\text{first}}$, and $\Delta G[H_iH_O]^{\text{second}}$, which have higher energies by 8–17 kJ mol^{-1}, corresponding 1000–2000 K. The $\Delta G[2H_i]$ values are much higher than $\Delta G[2H_O]^{\text{first}}$. These indicate that the $[2H_O]$ and $[H_iH_O]$ structures are dominant in SFOH. This preference can be rationalized in terms of the formation of CaO and H_2.

The exothermic conversion of CaH_2 to CaO is essential to the negative ΔG values. According to Figure 3-6, the formation of $[2H_O]$ and $[H_iH_O]$ structures produces larger amounts of CaO and H_2, and thus releases more heat.

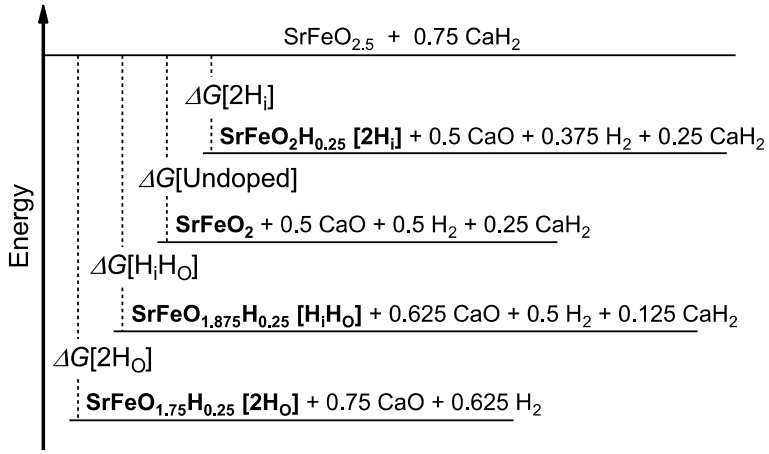

Figure 3-6. Schematic energy diagram of the hydrogenation reaction for H-doped $SrFeO_2$. The chemical formulas of reactants and products are shown for three types of H-doped $SrFeO_2$ and undoped $SrFeO_2$. The change of Gibbs energy though the reaction ($\Delta G[X]$) is defined as the energy differences between reactants and products.

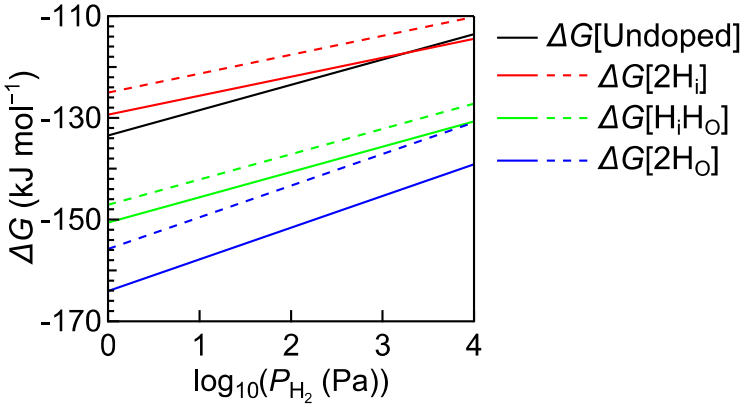

Figure 3-7. Calculated $\Delta G[X]$ values as a function of the partial pressure of H_2. For X = $2H_i$, $2H_O$, and H_iH_O, solid (dashed) lines correspond to the formation of the $[X]^{first}$ ($[X]^{second}$) structures in Figure 3-3.

From Table 3-2 and Figure 3-7, it is expected that the SFOH films contain large amounts of Fe^{+} and $Fe^{1.5+}$. Such anomalously reduced states of transition metals have been found in transition metal oxides prepared by topochemical methods, including Co^{+} and Co^{2+} in $LaSrCoO_{3.5-x}$ and Ni^{+} in $LaNiO_2$ [97,98]. Mössbauer spectroscopy of F-doped $SrFeO_2$ ($Sr_{1-\delta}FeO_{2-x}F_x$) revealed the presence of monovalent Fe [99]. However, the Fe-2*p* XPS spectrum of the SFOH film resembles that of Fe^{2+} with a similar binding energy [23], although the XPS spectrum of the Fe(I) compound is not well established. Thus, it is possible that the actual amount of Fe^{+} is less than that evaluated in Table 3-2 due to kinetic effects. For example, if the energy barrier for a hydrogen atom to substitute an O-site oxygen is much higher than that of the insertion process, the formation of $[2H_O]$ structures is suppressed. In this case, the secondary stable $[H_iH_O]$ structures with Fe^{2+} would be the primary component in the SFOH, which is consistent with the XPS results.

As seen from Figure 3-7, the energy differences between $[2H_O]^{first}$, $[2H_O]^{second}$, $[H_iH_O]^{first}$, and $[H_iH_O]^{second}$ are <20 kJ mol^{-1}, which is comparable with the thermal energy around the reaction temperature (240–280 °C) [23], suggesting that these four phases coexist in the SFOH films obtained by the hydridation of $SrFeO_{3-\delta}$ with CaH_2. This result leads to a two-phase model in which SFOH is composed of an insulating primary phase, $[2H_O]^{first}/[H_iH_O]^{first}$, and a metallic secondary phase, $[2H_O]^{second}/[H_iH_O]^{second}$. The ratio of these two phases can be estimated from the difference in ΔG and the reaction temperature of T = 520 K as $[2H_O]^{first}/[H_iH_O]^{first}$ (insulating): $[2H_O]^{second}/[H_iH_O]^{second}$ (metallic) ≈ 0.85:0.15. The formation of a connected network of metallic clusters in the insulating matrix could account not only for the high electric conduction but also for the small amount of carrier electrons observed in the experiment [23].

3.4. Conclusion

I proposed the crystal and electronic structures of H-doped $SrFeO_2$ considering the stability of various phases with different hydrogen configurations, including interstitial hydrogen filling the missing apical oxygen site, and hydrogen substituting the lattice oxygen site. The doped hydrogen was found to exist as hydride regardless of its spatial location in the crystal. The doped hydrogen drastically changed the energy position and occupation state of the minor-spin d_{zx} and d_z^2 bands of the adjacent iron atoms. As a result, either an insulating electronic band structure with a finite bandgap or a metallic band structure with fine density of state at the Fermi level was presented, depending on the arrangement of the incorporated hydride ions. Thermodynamic analysis revealed that an insulating SFOH phase with O-site hydride was preferably formed, but less stable metallic phases could also coexist. Percolation of the metallic domains explains the metallic transport and low carrier density experimentally observed.

Chapter 4. Metal-to-insulator transition of $NdNiO_3$ by fluorine doping

4.1. Introduction

In recent decades, progress in synthesis and characterization of mixed-anion oxides have been constructing an active research field in materials chemistry [5]. A popular approach is modification of existing oxides by doping other anions such as H^-, N^{3-}, and F^-. Especially, transition metal oxides with perovskite structure ABO_3 have been frequently selected as starting materials because of their abundant physical properties such as magnetism and metal-insulator transition [1]. So far, a variety of perovskite oxyhydrides, oxynitrides, and oxyfluorides have been synthesized and their unique properties have been unveiled [5,6]. Particularly, perovskite oxyfluorides $ABO_{3-x}F_x$ have been obtained by means of powder sintering, high-pressure/high-temperature synthesis, and topotactic reactions using polyvinylidene fluoride (PVDF) or XeF_2. So far, a series of perovskite oxyfluorides containing Sc [44,45], Ti [26], Mn [46,47], Fe [40–43,48–58], and Nb [60] at the *B*-site have been synthesized, and attracting physical properties such as strong antiferromagnetic interaction in $SrFeO_2F$ [50] have been reported.

Recently, Onozuka *et al.* reported a metal-to-insulator transition of a perovskite nickel oxide $NdNiO_3$ by fluorine substitution [59]. In this report, a thin film of metallic $NdNiO_3$ was fabricated by the pulsed-laser deposition (PLD) method and then fluorinated by the topotactic reaction using PVDF. The obtained $NdNiO_2F$ film has resistivity 10^7 times larger than that of the precursor $NdNiO_3$ at room temperature. Such colossal resistivity switching in Ni oxides has been also observed by proton insertion or

introduction of oxygen vacancies into RNiO$_3$ (R = La, Nd, Sm, or Eu) [100,101], but this is the first case with fluorine substitution and thus contribution of crystal field splitting is of interest. However, the local structure around Ni atoms in $NdNiO_2F$ thin films has not been determined because conventional structure-analysis methods such as Rietveld refinement cannot be applied to thin films due to their small volume and large background signals from substrates. Accordingly, detailed mechanisms of the metal-insulator transition have not been discussed yet.

In this study, I investigated crystal and electronic structures of $NdNiO_2F$ by band calculation based on the density functional theory. I found that that the doped fluorine atoms favor the specific oxygen site of $NdNiO_3$ and *cis* configuration. The origin of this positional preference was discussed using a simple ionic model. The experimental lattice constants and the band gap of $NdNiO_2F$ thin film were reproduced by the calculation considering a strain from the substrate. Subsequent band structure analysis showed that the divalent Ni ion in $NdNiO_2F$ has $e_g^{\uparrow\uparrow}$ configuration which favors an insulating electronic band structure due to strong intra-atomic Coulomb repulsion.

4.2. Calculation method

The crystal structure of $NdNiO_2F$ was determined by exhaustive structural sampling. The candidate structures were prepared by substituting fluorine atoms for 1/3 of oxygen atoms in the precursor $NdNiO_3$, which has a largely distorted orthorhombic structure with two symmetrically distinct groups of oxygen atoms: 4*c* and 8*d* (Figure 4-1) [102]. In this study, I used the simple-orthorhombic Bravais lattice of $NdNiO_2F$ which is a $\sqrt{2} \times \sqrt{2} \times 2$ supercell of the pseudo-cubic cell and contains 12 oxygen atoms. From the ${}_{12}C_4 = 495$ ways of substitution, I selected structures in which all the octahedra

have the composition NiO_4F_2 and removed duplicates. Eventually, the number of candidates was reduced to 22. Among them, 17 are constructed by *cis*-type NiO_4F_2 octahedra, 3 are *trans*-type, and the other 2 have both *cis*- and *trans*-type octahedra. Their lattice constants and atomic positions were optimized so that residual force on the atoms and stress on the cells were smaller than 0.01 eV/Å and 0.05 GPa, respectively. Then total energy and electronic band structures were examined. As for magnetic orderings of Ni^{2+} ions, three types of antiferromagnetic states (G/A/C-AFM) and a ferromagnetic state were considered.

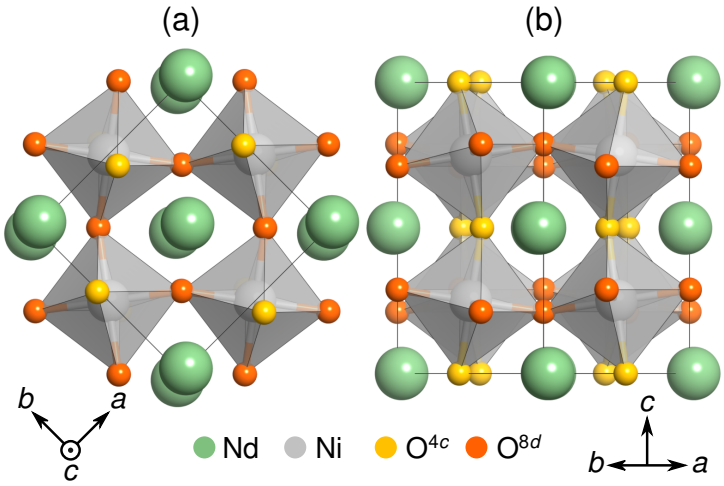

Figure 4-1. (a) Top and (b) side view of the crystal structure of $NdNiO_3$ with the orthorhombic (*Pbnm*) symmetry. The oxygen atoms are distinguished with their Wyckoff position: 4*c* or 8*d*.

The calculations were performed using the Vienna Ab initio Simulation Package [84]. The generalized gradient approximation by Perdew, Burke, and Ernzerhof [77] was used for the exchange-correlation functional. The localized nature of *d* electrons in Ni was treated by GGA+*U* method [85]. In this thesis, I employed a *U* value of 2.0 eV which is in the best agreement with the experimental observations, i.e., lattice constants and band gap. A plane-wave basis set with a cutoff energy of 800 eV was used

for the valence states including $5s^2 5p^6 6s^2$ of Nd, $3p^6 3d^8 4s^2$ of Ni, $2s^2 2p^4$ of O, and $2s^2 2p^5$ of F. The other core electrons were treated by the projector augmented wave method [82,86]. In this study, the localized 4*f* electrons of Nd were also kept frozen in the core like a previous theoretical work on $NdNiO_3$ [103]. The Brillouin zone integration was carried out by the Monkhorst-Pack scheme [83]. I used Γ-centered $3 \times 3 \times 2$ **k**-point mesh for the $\sqrt{2} \times \sqrt{2} \times 2$ supercells and $2 \times 2 \times 2$ mesh for auxiliary $2 \times 2 \times 2$ supercells. The crystal structures were visualized by VESTA [4].

4.3. Results and discussion

Figure 4-2 compares energy of the 22 structures calculated assuming G-type antiferromagnetism. They are divided into three groups according to the position of fluorine atoms. The first group consists of only one *trans*-structure with fluorine atoms at the 4*c* site (Figure 4-2(a)). The second is a group of 12 *cis*-structures with fluorine atoms at the both anion sites ($cis^{4c/8d}$ in Figure 4-2(b)). The last group, with fluorine atoms at only the 8*d* site, consists of five *cis*-, two *trans*-, and two *cis*/*trans*-structures (Figure 4-2(c)). It is shown that the *trans*-structures have the highest energy values no matter where the fluorine atoms are. In contrast, the energy of *cis*-structures depends on the position of fluorine atoms. It was found that the five *cis* structures with fluorine atoms at the 8*d* site are especially stable (cis^{8d} in Figure 4-2(c)).

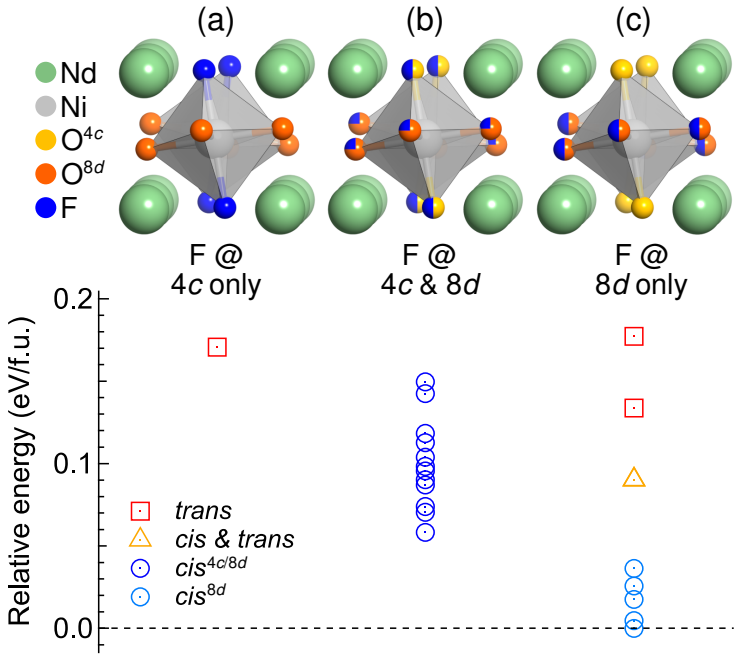

Figure 4-2. Total energy of the 22 structures calculated with the G-type antiferromagnetic order. They are grouped according to the position of fluorine atoms.

Relative energy with other magnetic orders were also examined. Figure 4-3 shows antiferromagnetic (AFM) and ferromagnetic (FM) orderings which can be realized in the unit cell used in this study, and energy of the 22 structures calculated with them. It indicates that the magnetic orderings do not affect the superior stability of the cis^{8d} structures followed by $cis^{4c/8d}$, *cis* & *trans*, and *trans* groups. Meanwhile a whole energy profile shifts towards higher energy region in the order of G-AFM < C-AFM < A-AFM < FM. As a result, the cis^{8d} structures with G-type AFM are most stable among all the structures and magnetisms. The G-AFM ordering, where neighboring spins have opposite orientations, is frequently observed in insulating transition metal oxides [1]. As such, it was predicted to be most likely for the insulating $NdNiO_2F$. The following part shows the results calculated with the G-type AFM.

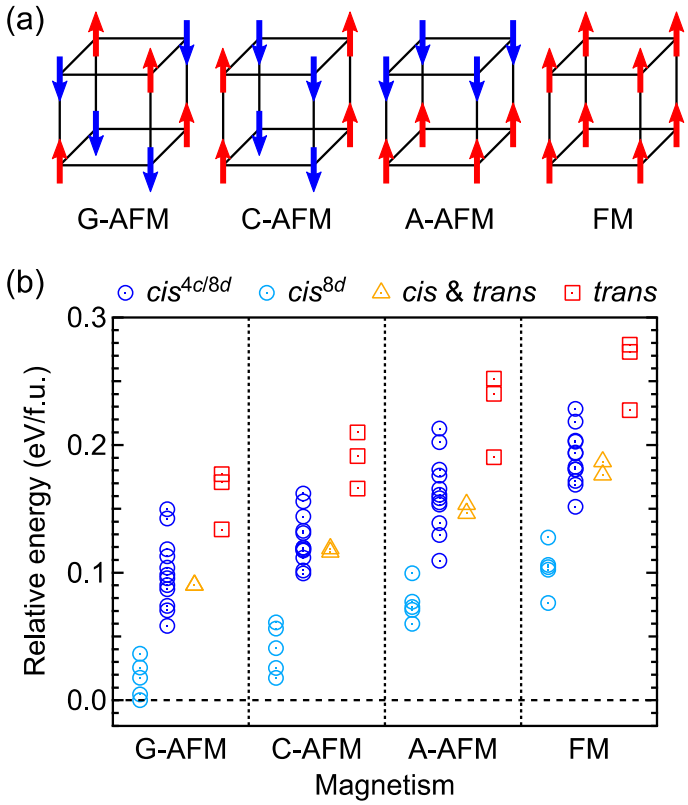

Figure 4-3. (a) Schemitic images for the four type of magnetic orderings. (b) Relative total energy of the 22 structures calculated with different magnetic orderings.

Figure 4-4 shows the most stable structure among the cis^{8d} group. Compared with the precursor $NdNi^{3+}O_3$ (Figure 4-1), the alternating displacement of *A*-site Nd atoms and the $a^-a^-c^+$-type rotation of octahedra are enhanced in the $NdNi^{2+}O_2F$. This is due to the larger ionic radius of Ni^{2+} than Ni^{3+} and the consequent smaller tolerance factor. As for anion ordering, O^{8d} and F atoms form a stripe pattern along the *a*-axis (Figure 4-4(a)). The other four cis^{8d} structures have the same ordering, though orientations are different. Because the $\sqrt{2} \times \sqrt{2} \times 2$ supercell used in the structure screening allows only this stripe pattern, it is unclear whether the stripe pattern is especially stable, or other O^{8d}/F orderings are also stable. To clarify this, I extended the size of the cell to $2 \times 2 \times 2$ and calculated the energy of additional 19 *cis* structures with different kinds of O^{8d}/F orderings. It was

found that the energy values of additional structures were in the same range as the five cis^{8d} structures (Figure 4-5). Hence, $NdNiO_2F$ does not have a specific preference to the stripe pattern. The replacement of the 8*d* oxygen and the *cis* configuration are dominant for stability.

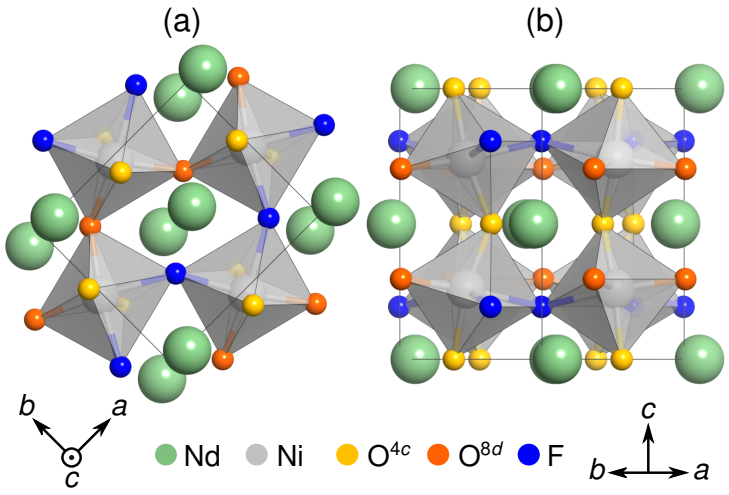

Figure 4-4. (a) Top and (b) side view of the most stable cis^{8d} structure.

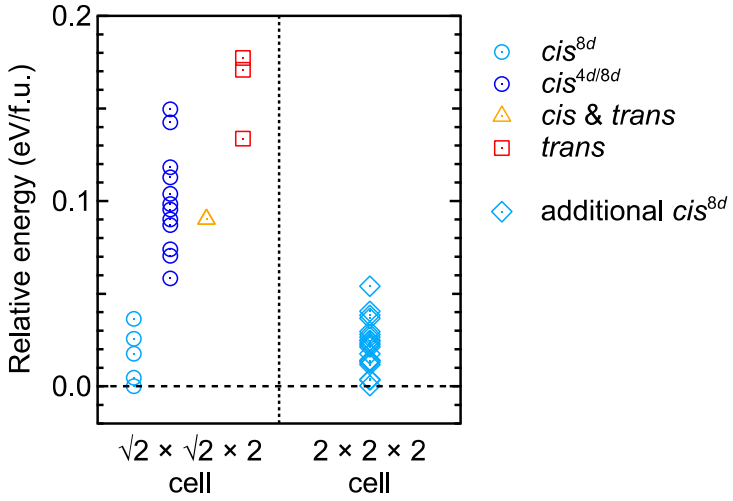

Figure 4-5. Relative total energy of the additional *cis* structures with the 2 × 2 × 2 supercell compared with the main 22 structures.

To discuss the origin of the structural selectivity, I investigated the main factor governing the characteristic structure, and found that a simple ionic model reproduces the order of the DFT total energy of the 22 structures. Figure 4-6(a) shows the relationship between the energy by the DFT calculation (E_{DFT}) and the Madelung energy:

$$E_{\mathrm{Madelung}} = \frac{e^2}{4\pi\varepsilon_0}\sum\frac{q_i q_j}{r_{ij}} \tag{4.1}$$

where the atoms are approximated as point charges q_i and the Coulomb potentials between all the (i, j) pairs are summed up. I used nominal charge numbers of ions ($q_{\mathrm{Nd}} = +3$, $q_{\mathrm{Ni}} = +2$, $q_{\mathrm{O}} = -2$, and $q_{\mathrm{F}} = -1$) and structures optimized by the DFT calculation to calculate inter-atomic distance r_{ij}. The linear relationship between E_{Madelung} and E_{DFT} indicates that this ionic model well describes the actual stability. In other words, the atoms in $NdNiO_2F$ behave as charged rigid spheres and optimize their positions so that the electrostatic energy becomes as low as possible with given fluorine positions.

For further discussion, I examined the Ni–anion bond lengths because they are the shortest bonds and thus largely contribute to E_{Madelung}. Figure 4-6(b) shows Ni–O/F bond ranges in the stable structures. They are divided into shorter Ni–O and longer Ni–F. In terms of the ionic model, this behavior can be understood by stronger attractive Coulomb force between Ni^{2+} and O^{2-} than between Ni^{2+} and F^-. This bond polarization is significant in the *cis*^{8d} structures; the range of Ni–O bonds is narrow and there are clear gaps of >0.1 Å between Ni–O and Ni–F. The uniformly short Ni–O lengths in the *cis*^{8d} structures should be a key to the stability because they efficiently generate largely negative $q_{\mathrm{Ni}}q_{\mathrm{O}}/r_{\mathrm{Ni–O}}$ terms. In other words, the *cis*-type fluorine occupation on the 8*d* site of the orthorhombic perovskite realizes ideal bond polarization, and thus acquires the lowest energy values.

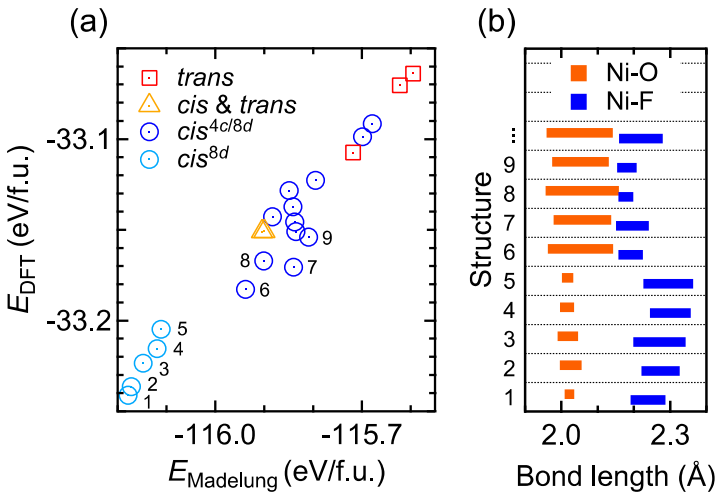

Figure 4-6. (a) Relationship between the Madelung energy and the total energy by the DFT calculation. (b) Range of Ni–O/F bond lengths in the stable structures.

The most stable cis^{8d} structure has an orthorhombic lattice with a = 5.99 Å, b = 5.44 Å and c = 7.70 Å, which can be converted into $a = b$ = 4.05 Å and c = 3.85 Å in the pseudo-cubic representation. These lattice constants are quite different from the experimental values: $a = b$ = 3.905 Å and c = 4.06 Å because the actual $NdNiO_2F$ thin film fabricated on the $SrTiO_3$ (100) substrate underwent epitaxial strain from the substrate, resulting in the compressed in-plane lattice constants [59]. Accordingly, I re-calculated the energy and lattice constants of $NdNiO_2F$ with the substrate strain and the growth orientations of the films taken into consideration.

Figure 4-7 shows a schematic image of $NdNiO_2F$ on the substrate. I considered a cubic perovskite (100) substrate with a lattice constant of 3.9 Å (the red mesh in Figure 4-7(b–d)). The $NdNiO_2F$ cells were transformed from $\sqrt{2} \times \sqrt{2} \times 2$ to $2 \times 2 \times 2$ so that all the three crystal faces A, B, and C match with the perovskite (100) surface. Then, they were optimized with two lattice constants (c.g. *ab*, *bc*, or *ca*) fixed to 7.8 Å square. Figure 4-7 shows the optimized lattice constants and the energy values of the most stable cis^{8d} structure. It was found that the orientations on A/B-faces are more stable than C-based

one. This is due to the anisotropic lattice constants of the free-standing cis^{8d} structure: $a = b = 8.09$ Å and $c = 7.70$ Å (Figure 4-7(a)). In the case of C-face locking, both the larger a- and b-axis are compressed to 7.8 Å and thus the system becomes more unstable. This anisotropic response also results in a large difference in the out-of-plane lattice constants: 7.97 Å and 8.15 Å for C- and A/B-based structures, respectively.

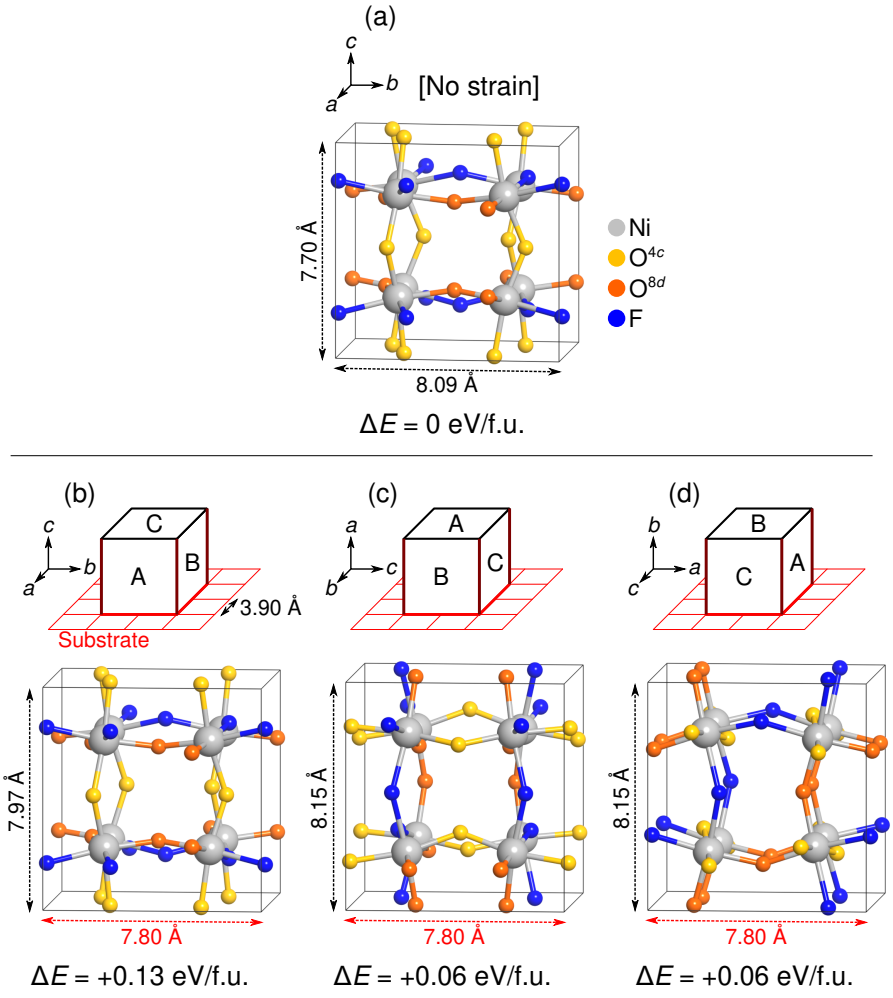

Figure 4-7. Results of structure optimizations of the most stable cis^{8d} structure with/without the substrate strain. (a) Free-standing. (b–d) The crystal face C/A/B is down and locked by substrate. Nd atoms are omitted for simplicity.

Figure 4-8 summarizes the energy comparison between the 22 structures with the confined lattice and three orientations. It shows that the cis^{8d} structures are more sensitive to growth orientations than other $cis^{4c/8d}$ structures. This is due to the selective occupation of fluorine atoms at the 8*d* site and consequent anisotropic lattice constants as discussed in Figure 4-7. However, the superior stability of the cis^{8d} structures remained in any orientations. Consequently, the actual $NdNiO_2F$ thin films are supposed to have the cis^{8d} structure with A/B-based orientations. The calculated out-of-plane lattice constant is 8.15 Å, i.e. 4.075 Å in the pseudo-cubic representation (Figure 4-7(c–d)), which is indeed in good agreement with the experimental value (4.06 Å).

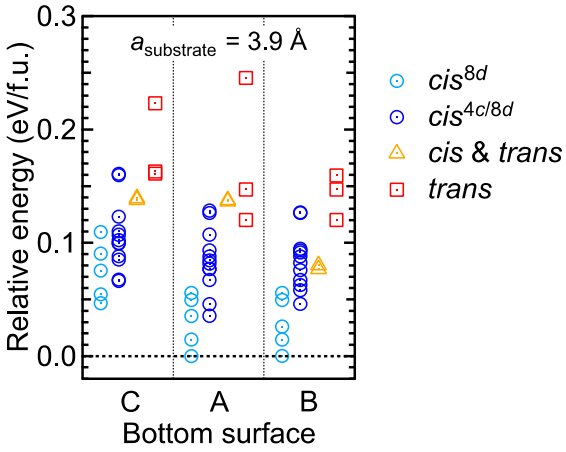

Figure 4-8. Total energy of the 22 structures calculated assuming strain from substrate.

Finally, the electronic structure of $NdNiO_2F$ was investigated using the results of the structure sampling. Figure 4-9(a) shows the band dispersion of the most stable cis^{8d} structure (Figure 4-4). The GGA + U (U = 2.0 eV) calculation predicted an insulating band structure with a band gap of 2.0 eV. Moreover, the direct and indirect band gap values are almost identical because the dispersion of the valence and conduction bands is very small. Therefore, $NdNiO_2F$ can be regarded as an insulator with a direct band gap of

2.0 eV, which is in good agreement with the result of optical measurements for the $NdNiO_2F$ thin films [59]. Figure 4-9(b) shows the calculated density of states (DOS). The valence band is constructed by the hybridized Ni/O bands and the isolated F band at the bottom. The isolation of the F band is due to the larger electronegativity of fluorine than oxygen, which not only makes the band position low but also suppresses the hybridization with Ni-3*d* states.

Next, the *d*-electron configuration of the Ni ion was examined because it is a key to understand the mechanism of the metal-insulator transition. Figure 4-9(c) shows calculated partial density of states (PDOS) for five *d*-orbitals of Ni^{2+} in the most stable cis^{8d} structure. Although the original symmetry of NiO_6 octahedra is broken by the *cis* configuration, the calculated PDOS indicates that the degeneracy of the t_{2g} and e_g orbitals is almost maintained, and that Ni^{2+} in $NdNiO_2F$ has the typical d^8 configuration for six-coordinated octahedra: $t_{2g}^6 e_g^{\uparrow\uparrow}$. Hence it follows that the fluorine doping has the same effect as proton doping and incorporation of oxygen vacancies: changing the occupation state of the e_g orbitals from $e_g^{\uparrow}$ to $e_g^{\uparrow\uparrow}$ [101]. The half occupied e_g orbital is unfavorable for electronic conduction because on-site Coulomb interaction prevents electrons from hopping to the neighboring Ni^{2+} cations. Such a correlated nature of Ni^{2+} ion manifested itself as the insulating electronic state of $NdNiO_2F$ revealed by the experiment and the theoretical calculation.

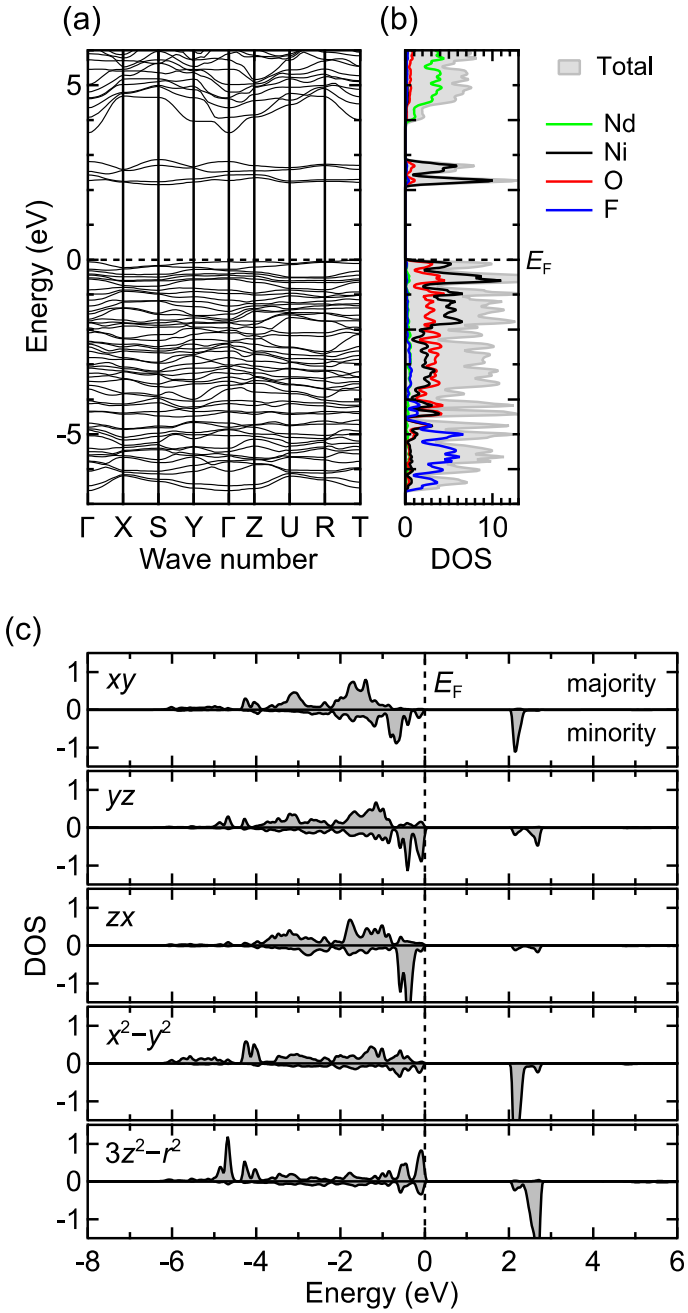

Figure 4-9. Calculated electronic states of the most stable *cis*^{8d} structure. (a) Band dispersion. (b) Density of states (DOS) for the total electrons and partial DOS for Nd, Ni, O, and F. (c) Partial DOS for 3*d* orbitals of Ni. Broken lines in the images depict the Fermi level (E_F).

4.4. Conclusion

The crystal and electronic structure of $NdNiO_2F$ were investigated using band calculations based on the density functional theory. The structural screening of $NdNiO_2F$ revealed that fluorine atoms prefer to *cis* configuration and the 8*d* site of the orthorhombic perovskite structure, resulting a two-dimensional fluorine distribution. The analysis using the Madelung energy suggested that this structural preference originates from the geometric property of the orthorhombic perovskite in which the cis^{8d} configuration realizes ideal bond polarization into shorter Ni–O and longer Ni–F and minimizes the electrostatic energy. The structure optimization including epitaxial strain and subsequent electronic state calculation reproduced both the experimental out-of-plane lattice constant and the insulating state of $NdNiO_2F$ with a direct band gap of 2.0 eV. The detailed analysis using partial density of states (PDOS) for 3*d* electrons showed that the Ni^{2+} in $NdNiO_2F$ has $t_{2g}^6 e_g^{\uparrow\uparrow}$ *d*-electron configuration, which precludes electron hopping due to the strong on-site Coulomb repulsion and causes the drastic resistivity increase.

Chapter 5. Metal-to-insulator transition of Sr_2RuO_4 by fluorine doping[†]

5.1. Introduction

Perovskite-type strontium ruthenates, Sr_2RuO_4, where layers of corner-sharing RuO_6 octahedra are separated by $(SrO)_2$ rock salt blocks, has attracted researchers' interest because of its novel electric properties. While Sr_2RuO_4 shows paramagnetic metallic behavior in room temperature, it undergoes a spin-triplet superconducting transition below 1.5 K [104]. The electronic and magnetic properties of Sr_2RuO_4 drastically change as Sr ions are gradually replaced by the isovalent Ca ions. First, the superconducting phase immediately disappears by the substitutions, owing to the narrowing of the bandwidth arising from the decrease in the Ru–O–Ru bond angles [105]. When the 3/4 of Sr atoms are replaced, a complex magnetism appears at low temperatures. Eventually, it transits to an insulator with antiferromagnetic orderings [70]. This diversity of electronic properties owes the orbital degree of freedom in the d^4 configuration of Ru^{4+}, which has a potentiality for electron rearrangement induced by external stimuli.

[†] This chapter contains the contents of the following publication.

"Spectroscopic and theoretical investigation of the electronic states of layered perovskite oxyfluoride $Sr_2RuO_3F_2$ thin films"
Akira Chikamatsu, Yuji Kurauchi, Keisuke Kawahara, Tomoya Onozuka, Makoto Minohara, Hiroshi Kumigashira, Eiji Ikenaga, and Tetsuya Hasegawa
Physical Review B **97**, 235101 (2018).

The electronic properties of strontium ruthenates can also be readily altered by anion doping. Recently, $Sr_2RuO_3F_2$ was synthesized in the form of epitaxial thin films by the topotactic fluorination of single-layered Sr_2RuO_4 precursor films using polyvinylidene fluoride (PVDF) [39]. In this reaction, both fluorine insertion into the $(SrO)_2$ blocks and the formation of oxygen vacancies in the O^{2-} sites of the RuO_6 octahedra are supposed to take place simultaneously, although experimental confirmation has not been achieved yet. While the oxidation state of Ru remains at 4+ after fluorination (redox-neutral), the $Sr_2RuO_3F_2$ thin film exhibits insulating behavior, with a resistivity of ~4.1×10 Ωcm at 300 K, which is five orders of magnitude higher than that of the metallic Sr_2RuO_4 film (~6.7×10^{-4} Ωcm). To unveil the origin of the metal-insulator transition of $Sr_2RuO_3F_2$, theoretical approaches to investigate the electronic states of $Sr_2RuO_3F_2$ are highly desirable.

In this study, the crystal and electronic structure of a $Sr_2RuO_3F_2$ thin film and the origin of the metal-insulator transition were investigated by density functional theory (DFT)-based calculations. The experimental lattice constants and insulating electronic structure of $Sr_2RuO_3F_2$ were reproduced by using the crystal structure of $Sr_2TiO_3F_2$ and GGA + U method with a carefully chosen U value. The density of states (DOS) calculations showed that the d electron configuration of Ru^{4+} (d^4) changed from (xy, yz, zx)^4 to $(xy)^{\uparrow}(yz, zx)^{\uparrow\uparrow}(3z^2-r^2)^{\uparrow}$ by fluorination, which causes the transition from metal to insulator.

5.2. Calculation method

In this study, I assumed that $Sr_2RuO_3F_2$ has the same crystal structure as $Sr_2TiO_3F_2$ [34] (Figure 5-1(a)) and optimized the lattice constants and atomic positions so that the residual force on an atom and the pressure on the cell were smaller than 0.01 eV $Å^{-1}$ and 0.1 GPa, respectively. As for magnetism, two types of in-plane ordering were considered for Ru^{4+} spins, "check type" and "plain type" (Figure 5-1(b)) and ignored interlayer orderings because preliminary calculations showed that interlayer magnetic couplings were negligibly small (~0.05 kJ/mol).

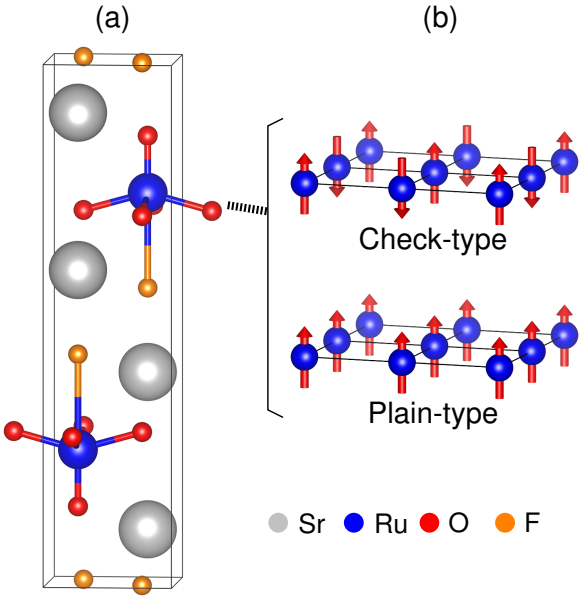

Figure 5-1. (a) $Sr_2RuO_3F_2$ with $Sr_2TiO_3F_2$-type structure. (b) Two types of in-plane magnetic orderings of Ru spins. Upward and downward arrows denote up- and down-spin moment, respectively.

DFT calculations were performed using the Vienna *ab initio* simulation package [84]. The generalized gradient approximation proposed by Perdew, Burke, and Ernzerhof (GGA-PBE) was adapted for the exchange correlation functional [77]. On-site Coulomb repulsion between the Ru 4*d* electrons was treated using the GGA + *U* method proposed by Dudarev *et al* [85], where the *U* value was varied in a range of 0–7 eV to examine the *U* dependence of the results. The effect of the core electrons was incorporated using a projector augmented wave (PAW) approach [82,86]. The cutoff energy was 600 eV for the valence electronic states composed of $4s^2 4p^6 5s^2$ electrons in Sr, $4p^6 4d^8 5s^2$ electrons in Ru, $2s^2 2p^4$ electrons in O, and $2s^2 2p^5$ electrons in F. The Brillouin-zone integration was carried out according to the Monkhorst-Pack **k**-point scheme [83]. 7 × 7 × 1 and 3 × 3 × 1 **k**-point meshes are used for 1 × 1 × 1 and √2 × √2 × 1 supercells, respectively. The crystal structures and wave functions were visualized using VESTA [4].

5.3. Results and discussion

Figure 5-2(a) shows the *c*-axis lengths of $Sr_2RuO_3F_2$ obtained for the two magnetic orderings and a series of *U* values. Notably, optimization starting with different initial *c*-axis lengths resulted in different structures. As seen from the figure, five structure phases with different *c*-axis lengths were predicted: check-A, -B, -C and plain-A, -B. Among them, check-A and plain-A, which appeared at *U* larger than 4 eV, well reproduce the experimental *c* length (16.7 Å). Figure 5-2(b) compares the relative energy of the five phases. The most stable phase was plain-B and the second one was check-A when $U >$ 4.5 eV. These results suggest that the metastable check-A phase was formed in the $Sr_2RuO_3F_2$ film.

U values around 2 eV have been used for first-principles calculation of Ru

oxides [71,106–108]. However, the experimental lattice constants of the $Sr_2RuO_3F_2$ film were reproduced only when U is larger than 4 eV. To confirm the validity of such a high-U value, I calculated U using the first-principles method proposed by Cococcioni *et al.* (see 2.2.1) [80]. This method also predicted that the optimal U value for this Ru system is as high as 6.0 eV. Therefore, I employed U = 6.0 eV in the following calculations.

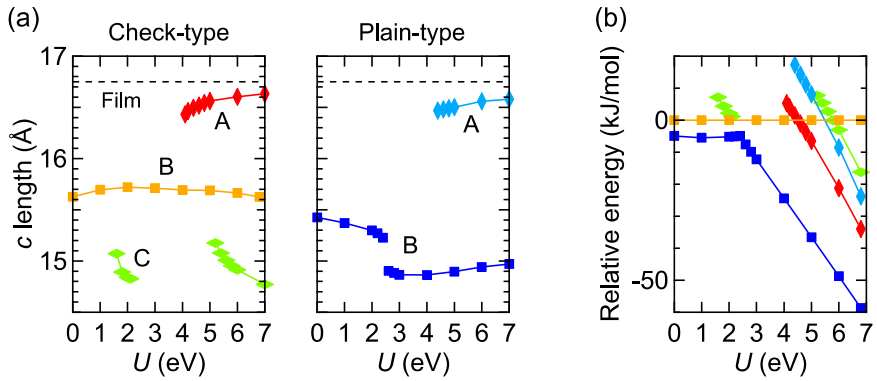

Figure 5-2. (a) c-axis lengths of $Sr_2RuO_3F_2$ calculated for various U values. The figures indicate five different phases: check-A, -B, -C and plain-A, -B. The experimental c-axis value is shown by a broken line. (b) Relative energy of the five phases as a function of U.

To understand why the most stable plain-B phase was not obtained in the actual film synthesis, I examined relative stability of the five phases as functions of in-plane lattice constant using the estimated U value (6.0 eV). Figure 5-3 shows the total energy of the five structural phases calculated with constrained in-plane lattice. The plain-B (blue) and check-A (red) phases have different optimal a-axis lengths: 4.00 Å and 3.85 Å, respectively. As a result, check-A becomes the most stable phase when a is shorter than 3.78 Å. The actual $Sr_2RuO_3F_2$ thin film was fabricated on the $LaAiO_3$ (100) substrate whose lattice constant is 3.79 Å. Therefore, it is possible that compressive strain from the $LaAiO_3$ substrate stabilizes the meta-stable check-A phase.

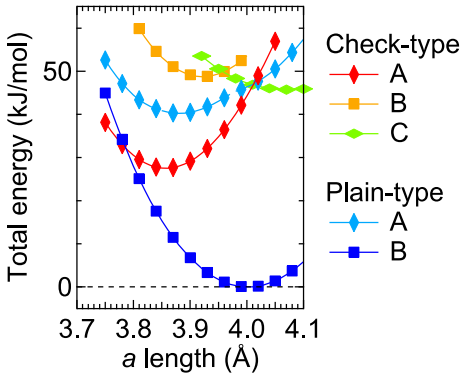

Figure 5-3. Relative total energy of the five structural phases calculated after constrained structure optimization where the in-plane (*a*-axis) lattice constant was fixed and the out-of-plane (*c*-axis) lattice constant was optimized. The theoretically estimated *U* value (6.0 eV) was used.

Figure 5-4(a) and (b) depict the crystal structure of Sr_2RuO_4 reported by Huang *et al*. [109] and the check-A structure of $Sr_2RuO_3F_2$ calculated by the GGA+*U* method. The calculated lattice constants are in good agreement with the experimentally measured constants (a = 3.86 Å and c = 16.75 Å) [39]. As shown in Figure 5-4(b), the center Ru cation in the RuO_5F octahedra of $Sr_2RuO_3F_2$ is displaced towards the more negative O^{2-} than F^-. As a result, the Ru-O bond lengths are as short as ~2 Å, being almost the same as those in Sr_2RuO_4 (Figure 5-4(a)) [109], whereas the Ru-F bond distance is elongated up to ~3 Å.

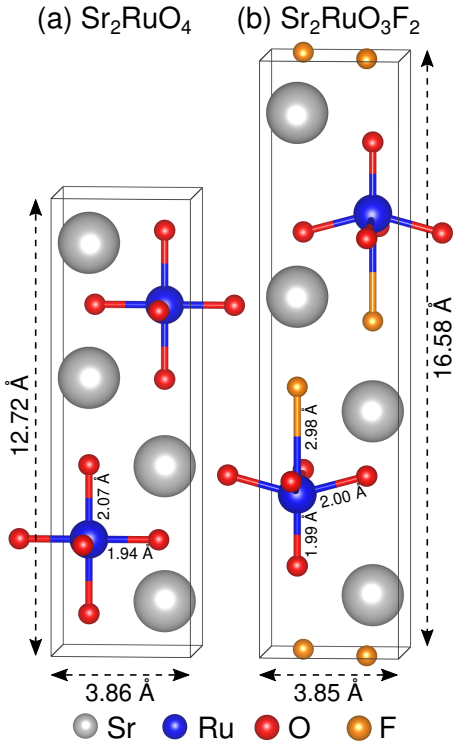

Figure 5-4. (a) The reported crystal structure of Sr_2RuO_4 in Ref. [109] and (b) the structure of $Sr_2RuO_3F_2$ calculated by the GGA+U method. The lattice constants and Ru-O/F bond lengths (Å) are shown in the figures.

Figure 5-5(a) depicts the DOS of Sr_2RuO_4 obtained by the GGA+U calculation, where the reported crystal structure [109], paramagnetism [70] and the U value of 5.3 eV estimated by the Cococcioni's procedure were used. As seen in Figure 5-5(a), the valence band of Sr_2RuO_4 is composed of Ru t_{2g}-derived states crossing the Fermi level E_F, O 2p bands located at –1.3 eV to –3.5 eV, isolated p_z orbitals of apical oxygen atoms hybridized with the Ru $3z^2–r^2$ orbital around –4 eV, and Ru 4d and O 2p derived states located at –4.2 eV to –7 eV. The valence band qualitatively reproduced a previous calculation accomplished by local-density approximation (LDA) [110]. Figure 5-5(b) shows the calculated DOS for $Sr_2RuO_3F_2$. Remarkably, a finite gap opened at E_F and the Ru 4d states moved to the bottom of the valence bands near –8 eV. Furthermore, the F 2p states

appeared at –3 to –6.5 eV; they were almost isolated and not hybridized with the Ru 4*d* states, reflecting the long bond distance between Ru and F.

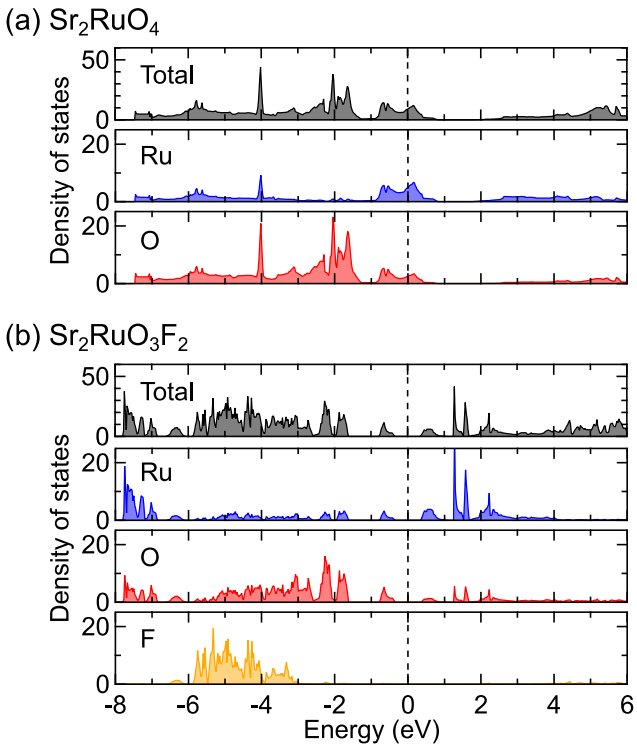

Figure 5-5. Total and site-projected DOS for (a) Sr_2RuO_4 and (b) $Sr_2RuO_3F_2$. The vertical dashed lines denote the fermi level E_F.

Figure 5-6 shows the calculated band dispersion of $Sr_2RuO_3F_2$ with the Brillouin zone for a simple tetragonal lattice. As seen in the figure, $Sr_2RuO_3F_2$ has little dispersion along the Γ–Z path and the band structures along Γ–*X*–*M* (k_z = 0) and *Z*–*R*–*A* (k_z = 1/2) are almost identical because of the long *c*-axis. The valence band maximum is located at the points *M* and *A* while the conduction minimum is at *X* and *R*, suggesting that $Sr_2RuO_3F_2$ has an indirect band gap. The width of the band gap was estimated to be 0.7 eV.

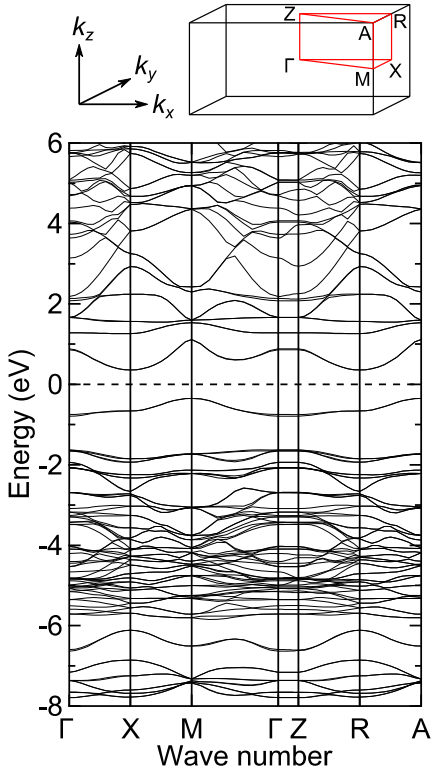

Figure 5-6. Band dispersion image of $Sr_2RuO_3F_2$ and the Brillouin zone for a simple tetragonal lattice; the critical points are denoted. The horizontal dashed line in the lower illustration denotes E_F.

In order to investigate the *d* electron configuration of Ru^{4+} (d^4) in Sr_2RuO_4 and $Sr_2RuO_3F_2$, I calculated the partial DOS (PDOS) for the five *d* bands of Ru, as shown in Figure 5-7. Ru^{4+} oxides with octahedral geometry are usually a low-spin configuration $(xy, yz, zx)^{\uparrow\uparrow\uparrow\downarrow}$, such as $SrRuO_3$ and Ca_2RuO_4 [111,112], or non-spin-polarized $(xy, yz, zx)^4$, such as Sr_2RuO_4 and RuO_2 [70,113]. In these compounds, the fourth *d* electron occupies not an e_g band, but a t_{2g} band, due to the large crystal-field splitting between the t_{2g} and e_g orbitals. Figure 5-7(a) shows PDOS for Sr_2RuO_4. It depicts the t_{2g}^4 configuration as reported in Ref. 71. In this case, the occupation number of electrons per band is 4/3 and thus the system is metallic. However, PDOS for $Sr_2RuO_3F_2$ (Figure 5-7(b)) suggests the

Ru^{4+} exhibited a high-spin configuration, $(xy)^{\uparrow}(yz,zx)^{\uparrow\uparrow}(3z^2-r^2)^{\uparrow}$. Accordingly, the occupation number per band also changed from non-integer 4/3 to integer 1, resulting in the metal-insulator transition.

This anomalous occupation of the $(3z^2-r^2)^{\uparrow}$ orbital would be due to the change in crystal field around Ru atoms. Figure 5-8 shows the local geometries around Ru of the two compounds shown in Figs. Figure 5-4(a) and Figure 5-4(b), and the schematic energy diagrams for the *d* orbitals. Sr_2RuO_4 has almost regular RuO_6 octahedra and well separated t_{2g} and e_g orbitals, and all four *d* electrons of Sr_2RuO_4 occupy the t_{2g} band. On the other hand, $Sr_2RuO_3F_2$ has long Ru–F bond distance, which makes the coordination geometry of Ru square pyramidal-like rather than octahedral, and thus stabilizes the $3z^2-r^2$ orbital. As a result, the fourth electron occupies the $3z^2-r^2$ orbital, and the whole configuration becomes the high-spin state.

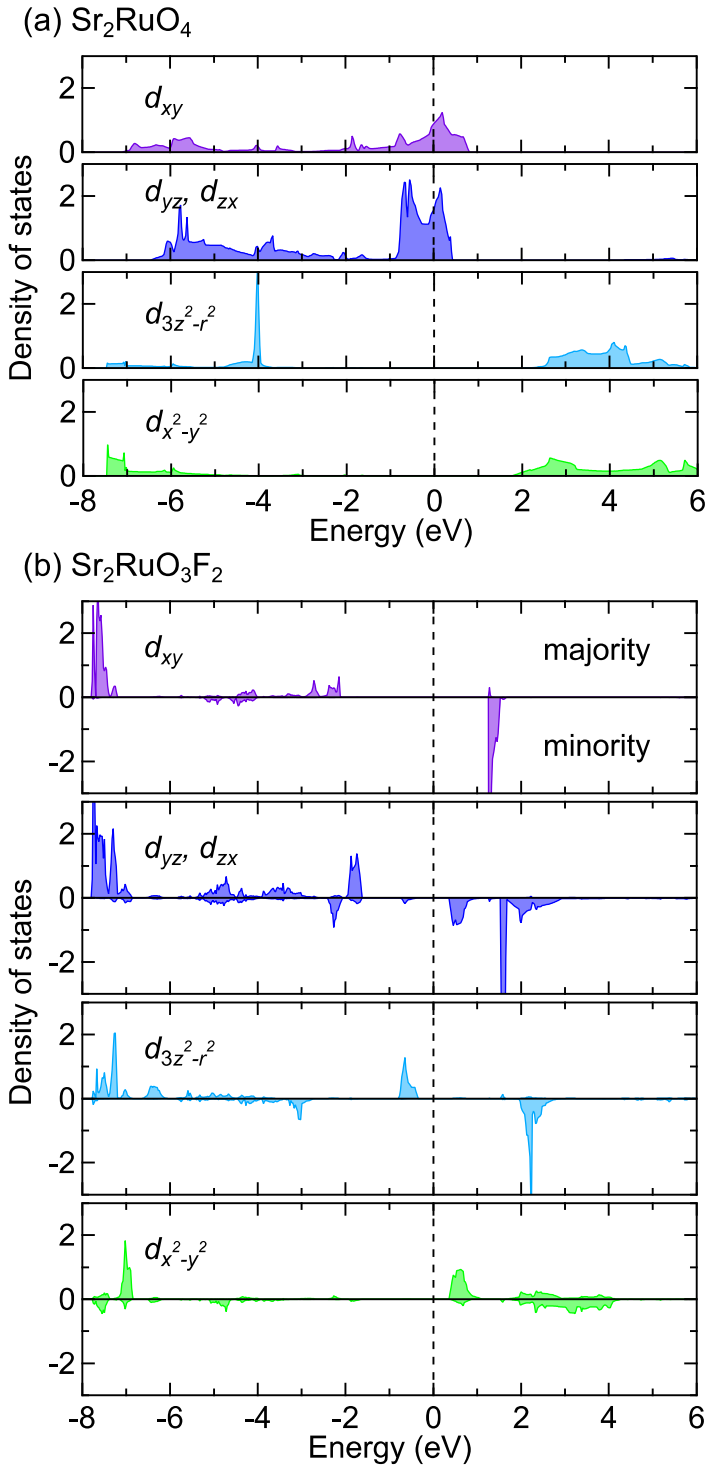

Figure 5-7. PDOS for the Ru-4*d* electrons in (a) Sr_2RuO_4 and (b) $Sr_2RuO_3F_2$. The lines in positive and negative regions denote the PDOS of majority and minority of spin electrons, respectively.

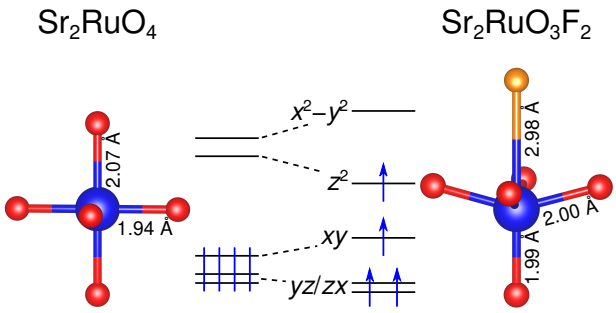

Figure 5-8. The local structures around Ru in Sr_2RuO_4 and $Sr_2RuO_3F_2$, and the schematic diagrams for $4d^4$ configurations under the two types of crystal field.

5.4. Conclusion

The crystal and electronic structure of a $Sr_2RuO_3F_2$ thin film and the mechanism of the metal-insulator transition by F doping were investigated by the band calculation based on the density functional theory. The experimental lattice constants and electronic structures of both Sr_2RuO_4 and $Sr_2RuO_3F_2$ were reproduced by the GGA+*U* calculations. Further analysis using density of states (DOS) data predicted that $Sr_2RuO_3F_2$ has a high-spin Ru (IV) configuration and an indirect band gap of 0.7 eV with minima at *M*, *A* and *X*, *R* points while the result for the precursor oxide Sr_2RuO_4 showed the metallic band structure with the t_{2g}^4 electronic configuration. This electronic modification is possibly driven by the substitution of oxygen atoms coordinated to Ru by fluorine and resulting crystal field deviation.

Chapter 6. General conclusion

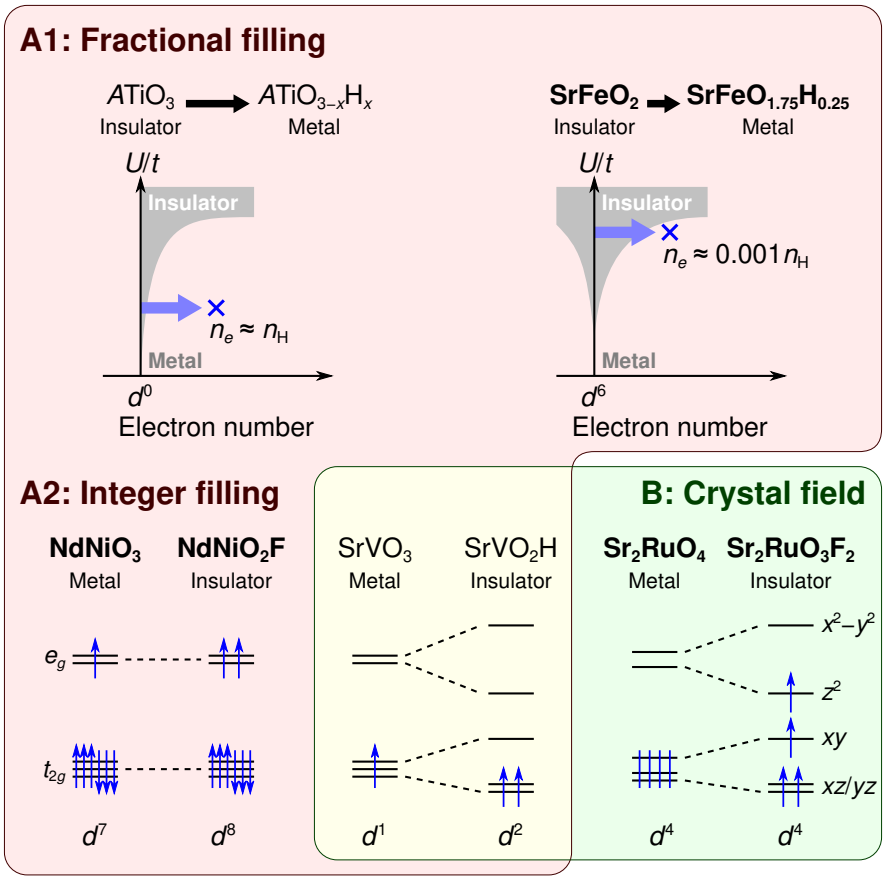

Figure 6-1. Schematic diagrams illustrating mechanisms of metal-insulator transitions induced by anion doping. (A1) Fractional electron doping by aliovalent substitution of hydride anions. n_e and n_H stand for the concentrations of carrier electrons and doped hydrogen, respectively. (A2) Integer electron doping by fluorine and hydride doping. (B) Crystal field splitting in Sr_2RuO_4 and $Sr_2RuO_3F_2$. The three cases written in the bold style ($SrFeO_{1.75}H_{0.25}$, $NdNiO_2F$, $Sr_2RuO_3F_2$) were studied in this thesis.

In this thesis, I theoretically studied the metal-insulator transitions (MIT) caused by anion doping to transition metal oxides: $SrFeO_2$, $NdNiO_3$, and Sr_2RuO_4. The investigation was accomplished through structural characterization and subsequent band structure analysis for the doped compounds: $SrFeO_xH_{0.24}$, $NdNiO_2F$, and $Sr_2RuO_3F_2$. With the achievements in this study, we can now draw an overall picture of MIT induced by anion doping. Figure 6-1 summarizes the five cases of MIT by anion doping. Three of them ($SrFeO_2$, $NdNiO_3$, and Sr_2RuO_4) are findings in this study and the others (ATiO$_3$ and $SrVO_3$) were previously reported. They are classified according to the mechanisms of MIT proposed in Chapter 1 (Figure 1-6): filling control and crystal field splitting by anion doping. The filling control is further classified into fractional filling and integer filling according to the number of doped electrons.

The insulator-to-metal transitions of ATiO$_3$ and $SrFeO_2$ are both triggered by fractional electron filling due to the aliovalent substitution of hydride (A1 in Figure 6-1). However, the numbers of active carrier electrons are very different between the two cases. In ATiO$_{3-x}$H$_x$, most of the doped electrons become conduction carriers, whereas they are localized at iron atoms adjacent to hydride anions in $SrFeO_{1.75}H_{0.25}$. This suppression of electron conduction in $SrFeO_{1.75}H_{0.25}$ suggests that the correlation factor U/t of Fe^{2+} is higher than that of Ti^{4+} because large U/t prevents doped electrons from hopping and reduces the number of effective carriers.

All the compounds in the other three cases have integer numbers of electrons in d orbitals. In these cases, the metal-to-insulator transitions are induced by changes in occupation state of each orbital from a fraction to an integer. This switching is caused by electron doping (A2 in Figure 6-1), crystal field splitting (B), or collaboration between them. For example, the transition of metallic $NdNiO_3$ to insulating $NdNiO_2F$ is due to

integer filling of the e_g orbitals. The occupation number of the e_g orbitals changes from 1/2 to 1. On the other hand, Sr_2RuO_4 and $Sr_2RuO_3F_2$ show a novel transition induced only by the crystal field splitting. In this case, the fluorine substitution changes the coordination geometry from octahedral to pyramidal, resulting in electronic re-configuration and integer occupation. The last case consisting of $SrVO_3$ and $SrVO_2H$ can be understood by combination of integer filling and crystal field splitting as explained in 1.2.2 (p. 17). The increment of *d* electron and split t_{2g} orbitals due to the *trans* arrangement realize the integer occupation.

In conclusion, this theoretical study contributes to construction of a systematized knowledge about the metal-insulator transition induced by anion doping. In the expanding research field of anion-doped metal oxides, this achievement would provide a new perspective to design functional anion-doped compounds.

Bibliography

[1] M. Imada, A. Fujimori, and Y. Tokura, Rev. Mod. Phys. **70**, 1039 (1998).

[2] M. P. M. Dean, G. Dellea, R. S. Springell, F. Yakhou-Harris, K. Kummer, N. B. Brookes, X. Liu, Y. J. Sun, J. Strle, T. Schmitt, L. Braicovich, G. Ghiringhelli, I. Božović, and J. P. Hill, Nat. Mater. **12**, 1019 (2013).

[3] A. S. Bhalla, R. Guo, and R. Roy, Mater. Res. Innov. **4**, 3 (2000).

[4] K. Momma and F. Izumi, J. Appl. Crystallogr. **44**, 1272 (2011).

[5] H. Kageyama, K. Hayashi, K. Maeda, J. P. Attfield, Z. Hiroi, J. M. Rondinelli, and K. R. Poeppelmeier, Nat. Commun. **9**, 772 (2018).

[6] Y. Kobayashi, Y. Tsujimoto, and H. Kageyama, Annu. Rev. Mater. Res. **48**, 303 (2018).

[7] C. G. Van de Walle, Phys. Rev. Lett. **85**, 1012 (2000).

[8] A. Janotti and C. G. Van De Walle, Nat. Mater. **6**, 44 (2007).

[9] M. A. Hayward, E. J. Cussen, J. B. Claridge, M. Bieringer, M. J. Rosseinsky, C. J. Kiely, S. J. Blundell, I. M. Marshall, and F. L. Pratt, Science **295**, 1882 (2002).

[10] T. Sakaguchi, Y. Kobayashi, T. Yajima, M. Ohkura, C. Tassel, F. Takeiri, S. Mitsuoka, H. Ohkubo, T. Yamamoto, J. Kim, N. Tsuji, A. Fujihara, Y. Matsushita, J. Hester, M. Avdeev, K. Ohoyama, and H. Kageyama, Inorg. Chem. **51**, 11371 (2012).

[11] Y. Kobayashi, O. J. Hernandez, T. Sakaguchi, T. Yajima, T. Roisnel, Y. Tsujimoto, M. Morita, Y. Noda, Y. Mogami, A. Kitada, M. Ohkura, S. Hosokawa, Z. Li, K. Hayashi, Y. Kusano, J. E. Kim, N. Tsuji, A. Fujiwara, Y. Matsushita, K.

Yoshimura, K. Takegoshi, M. Inoue, M. Takano, and H. Kageyama, Nat. Mater. **11**, 507 (2012).

[12] T. Yamamoto, R. Yoshii, G. Bouilly, Y. Kobayashi, K. Fujita, Y. Kususe, Y. Matsushita, K. Tanaka, and H. Kageyama, Inorg. Chem. **54**, 1501 (2015).

[13] F. Denis Romero, A. Leach, J. S. Möller, F. Foronda, S. J. Blundell, and M. a Hayward, Angew. Chemie Int. Ed. **53**, 7556 (2014).

[14] R. M. Helps, N. H. Rees, and M. A. Hayward, Inorg. Chem. **49**, 11062 (2010).

[15] R. Sato, H. Saitoh, N. Endo, S. Takagi, M. Matsuo, K. Aoki, and S. Orimo, Appl. Phys. Lett. **102**, 091901 (2013).

[16] S. Ayukawa, K. Ikeda, M. Kato, T. Noji, S. Orimo, and Y. Koike, J. Phys. Soc. Japan **81**, 034704 (2012).

[17] C. Tassel, Y. Goto, Y. Kuno, J. Hester, M. Green, Y. Kobayashi, and H. Kageyama, Angew. Chemie **126**, 10545 (2014).

[18] Y. Goto, C. Tassel, Y. Noda, O. Hernandez, C. J. Pickard, M. A. Green, H. Sakaebe, N. Taguchi, Y. Uchimoto, Y. Kobayashi, and H. Kageyama, Inorg. Chem. **56**, 4840 (2017).

[19] C. Tassel, Y. Goto, D. Watabe, Y. Tang, H. Lu, Y. Kuno, F. Takeiri, T. Yamamoto, C. M. Brown, J. Hester, Y. Kobayashi, and H. Kageyama, Angew. Chemie **128**, 9819 (2016).

[20] T. Yajima, A. Kitada, Y. Kobayashi, T. Sakaguchi, G. Bouilly, S. Kasahara, T. Terashima, M. Takano, and H. Kageyama, J. Am. Chem. Soc. **134**, 8782 (2012).

[21] T. Katayama, A. Chikamatsu, K. Yamada, K. Shigematsu, T. Onozuka, M. Minohara, H. Kumigashira, E. Ikenaga, and T. Hasegawa, J. Appl. Phys. **120**, 085305 (2016).

[22] J. Bang, S. Matsuishi, H. Hiraka, F. Fujisaki, T. Otomo, S. Maki, J. Yamaura, R. Kumai, Y. Murakami, and H. Hosono, J. Am. Chem. Soc. **136**, 7221 (2014).

[23] T. Katayama, A. Chikamatsu, Y. Hirose, H. Kumigashira, T. Fukumura, and T. Hasegawa, J. Phys. D. Appl. Phys. **47**, 135304 (2014).

[24] T. Katayama, A. Chikamatsu, H. Kamisaka, Y. Yokoyama, Y. Hirata, H. Wadati, T. Fukumura, and T. Hasegawa, AIP Adv. **5**, 107147 (2015).

[25] F. Galasso and W. Darby, J. Phys. Chem. **66**, 1318 (1962).

[26] B. L. Chamberland, Mater. Res. Bull. **6**, 311 (1971).

[27] P. R. Slater, J. Fluor. Chem. **117**, 43 (2002).

[28] Y. Wang, K. Tang, B. Zhu, D. Wang, Q. Hao, and Y. Wang, Mater. Res. Bull. **65**, 42 (2015).

[29] G. S. Case, A. L. Hector, W. Levason, R. L. Needs, M. F. Thomas, and M. T. Weller, J. Mater. Chem. **9**, 2821 (1999).

[30] Y. Su, Y. Tsujimoto, Y. Matsushita, Y. Yuan, J. He, and K. Yamaura, Inorg. Chem. **55**, 2627 (2016).

[31] Y. Tsujimoto, Y. Matsushita, N. Hayashi, K. Yamaura, and T. Uchikoshi, Cryst. Growth Des. **14**, 4278 (2014).

[32] Y. Tsujimoto, J. J. Li, K. Yamaura, Y. Matsushita, Y. Katsuya, M. Tanaka, Y. Shirako, M. Akaogi, and E. Takayama-Muromachi, Chem. Commun. **47**, 3263 (2011).

[33] Y. Tsujimoto, K. Yamaura, and T. Uchikoshi, Inorg. Chem. **52**, 10211 (2013).

[34] P. R. Slater and R. K. B. Gover, J. Mater. Chem. **12**, 291 (2002).

[35] K. Wissel, J. Heldt, P. B. Groszewicz, S. Dasgupta, H. Breitzke, M. Donzelli, A. I. Waidha, A. D. Fortes, J. Rohrer, P. R. Slater, G. Buntkowsky, and O. Clemens,

Inorg. Chem. **57**, 6549 (2018).

[36] P. R. Slater and R. K. B. Gover, J. Mater. Chem. **11**, 2035 (2001).

[37] M. AI-Mamouri, P. P. Edwards, C. Greaves, and M. Slaski, Nature **369**, 382 (1994).

[38] L. D. Aikens, R. K. Li, and C. Greaves, Chem. Commun. 2129 (2000).

[39] K. Kawahara, A. Chikamatsu, T. Katayama, T. Onozuka, D. Ogawa, K. Morikawa, E. Ikenaga, Y. Hirose, I. Harayama, D. Sekiba, T. Fukumura, and T. Hasegawa, CrystEngComm **19**, 313 (2017).

[40] O. Clemens, F. J. Berry, A. J. Wright, K. S. Knight, J. M. Perez-Mato, J. M. Igartua, and P. R. Slater, J. Solid State Chem. **206**, 158 (2013).

[41] C. M. Thompson, C. K. Blakely, R. Flacau, J. E. Greedan, and V. V. Poltavets, J. Solid State Chem. **219**, 173 (2014).

[42] C. M. Thompson, C. K. Blakely, R. Flacau, J. E. Greedan, and V. V. Poltavets, J. Solid State Chem. **226**, 332 (2015).

[43] O. Clemens, F. J. Berry, A. J. Wright, K. S. Knight, J. M. Perez-Mato, J. M. Igartua, and P. R. Slater, J. Solid State Chem. **226**, 326 (2015).

[44] R. L. Needs and M. T. Weller, J. Solid State Chem. **139**, 422 (1998).

[45] T. Katsumata, M. Nakashima, H. Umemoto, and Y. Inaguma, J. Solid State Chem. **181**, 2637 (2008).

[46] M. V. Lobanov, A. M. Abakumov, A. V. Sidorova, M. G. Rozova, O. G. D'yachenko, E. V. Antipov, J. Hadermann, and G. Van Tendeloo, Solid State Sci. **4**, 19 (2002).

[47] T. Katsumata, M. Nakashima, Y. Inaguma, and T. Tsurui, Bull. Chem. Soc. Jpn. **85**, 397 (2012).

[48] F. J. Berry, X. Ren, R. Heap, P. Slater, and M. F. Thomas, Solid State Commun.

134, 621 (2005).

[49] R. Heap, P. R. Slater, F. J. Berry, O. Helgason, and A. J. Wright, Solid State Commun. **141**, 467 (2007).

[50] F. J. Berry, R. Heap, Ö. Helgason, E. A. Moore, S. Shim, P. R. Slater, and M. F. Thomas, J. Phys. Condens. Matter **20**, (2008).

[51] O. Clemens, M. Kuhn, and R. Haberkorn, J. Solid State Chem. **184**, 2870 (2011).

[52] F. J. Berry, F. C. Coomer, C. Hancock, Ö. Helgason, E. A. Moore, P. R. Slater, A. J. Wright, and M. F. Thomas, J. Solid State Chem. **184**, 1361 (2011).

[53] C. K. Blakely, J. D. Davis, S. R. Bruno, S. K. Kraemer, M. Zhu, X. Ke, W. Bi, E. E. Alp, and V. V. Poltavets, J. Fluor. Chem. **159**, 8 (2014).

[54] E. J. Moon, Y. Xie, E. D. Laird, D. J. Keavney, C. Y. Li, and S. J. May, J. Am. Chem. Soc. **136**, 2224 (2014).

[55] T. Katayama, A. Chikamatsu, Y. Hirose, R. Takagi, H. Kamisaka, T. Fukumura, and T. Hasegawa, J. Mater. Chem. C **2**, 5350 (2014).

[56] T. Katayama, A. Chikamatsu, H. Kamisaka, H. Kumigashira, and T. Hasegawa, Appl. Phys. Express **9**, 025801 (2016).

[57] Y. Inaguma, J. M. Greneche, M. P. Crosnier-Lopez, T. Katsumata, Y. Calage, and J. L. Fourquet, Chem. Mater. **17**, 1386 (2005).

[58] F. Takeiri, T. Yamamoto, N. Hayashi, S. Hosokawa, K. Arai, J. Kikkawa, K. Ikeda, T. Honda, T. Otomo, C. Tassel, K. Kimoto, and H. Kageyama, Inorg. Chem. **57**, 6686 (2018).

[59] T. Onozuka, A. Chikamatsu, T. Katayama, Y. Hirose, I. Harayama, D. Sekiba, E. Ikenaga, M. Minohara, H. Kumigashira, and T. Hasegawa, ACS Appl. Mater. Interfaces **9**, 10882 (2017).

[60] W. Rüdorff and D. Krug, Zeitschrift Für Anorg. Und Allg. Chemie **329**, 211 (1964).

[61] L. Cario, C. Vaju, B. Corraze, V. Guiot, and E. Janod, Adv. Mater. **22**, 5193 (2010).

[62] J. A. Alonso, M. J. Martínez-Lope, M. T. Casais, M. A. G. Aranda, and M. T. Fernández-Díaz, J. Am. Chem. Soc. **121**, 4754 (1999).

[63] A. Muñoz, J. A. Alonso, M. J. Martínez-Lope, and M. T. Fernández-Díaz, J. Solid State Chem. **182**, 1982 (2009).

[64] J. A. Alonso, M. J. Martínez-Lope, I. A. Presniakov, A. V. Sobolev, V. S. Rusakov, A. M. Gapochka, G. Demazeau, and M. T. Fernández-Díaz, Phys. Rev. B **87**, 184111 (2013).

[65] M. L. Medarde, J. Phys. Condens. Matter **9**, 1679 (1997).

[66] J. A. Alonso, M. J. Martínez-Lope, M. T. Casais, J. L. García-Muñoz, M. T. Fernández-Díaz, and M. A. G. Aranda, Phys. Rev. B **64**, 094102 (2001).

[67] J. Alonso, M. Martínez-Lope, M. Casais, and J. García-Muñoz, Phys. Rev. B **61**, 1756 (2000).

[68] J. A. Alonso, M. J. Martínez-Lope, and I. Rasines, J. Solid State Chem. **120**, 170 (1995).

[69] J. B. Torrance, P. Lacorre, A. I. Nazzal, E. J. Ansaldo, and C. Niedermayer, Phys. Rev. B **45**, 8209 (1992).

[70] S. Nakatsuji and Y. Maeno, Phys. Rev. Lett. **84**, 2666 (2000).

[71] V. I. Anisimov, I. A. Nekrasov, D. E. Kondakov, T. M. Rice, and M. Sigrist, Eur. Phys. J. B **25**, 191 (2002).

[72] P. Steffens, O. Friedt, P. Alireza, W. G. Marshall, W. Schmidt, F. Nakamura, S. Nakatsuji, Y. Maeno, R. Lengsdorf, M. M. Abd-Elmeguid, and M. Braden, Phys. Rev. B **72**, 094104 (2005).

[73] Y. Wei, H. Gui, X. Li, Z. Zhao, Y.-H. Zhao, and W. Xie, J. Phys. Condens. Matter **27**, 206001 (2015).

[74] R. M. Martin, *Electronic Structure: Basic Theory and Practical Methods* (Cambridge University Press, 2008).

[75] P. Hohenberg and W. Kohn, Phys. Rev. **136**, B864 (1964).

[76] W. Kohn and L. J. Sham, Phys. Rev. **140**, A1133 (1965).

[77] J. P. Perdew, K. Burke, and M. Ernzerhof, Phys. Rev. Lett. **77**, 3865 (1996).

[78] J. Heyd, G. E. Scuseria, and M. Ernzerhof, J. Chem. Phys. **118**, 8207 (2003).

[79] V. I. Anisimov, J. Zaanen, and O. K. Andersen, Phys. Rev. B **44**, 943 (1991).

[80] M. Cococcioni and S. de Gironcoli, Phys. Rev. B **71**, 035105 (2005).

[81] J. F. Janak, Phys. Rev. B **18**, 7165 (1978).

[82] P. E. Blöchl, Phys. Rev. B **50**, 17953 (1994).

[83] H. Monkhorst and J. Pack, Phys. Rev. B **13**, 5188 (1976).

[84] G. Kresse and J. Furthmüller, Phys. Rev. B **54**, 11169 (1996).

[85] S. Dudarev and G. Botton, Phys. Rev. B **57**, 1505 (1998).

[86] G. Kresse, Phys. Rev. B **59**, 1758 (1999).

[87] T. Yamamoto and H. Kageyama, Chem. Lett. **42**, 946 (2013).

[88] J. Zhang, G. Gou, and B. Pan, J. Phys. Chem. C **118**, 17254 (2014).

[89] A. B. Bridges, G. R. Darling, M. A. Hayward, and M. J. Rosseinsky, J. Am. Chem. Soc. **127**, 5996 (2005).

[90] K. Liu, Y. Hou, X. Gong, and H. Xiang, Sci. Rep. **6**, 19653 (2016).

[91] Y. Tsujimoto, C. Tassel, N. Hayashi, T. Watanabe, H. Kageyama, K. Yoshimura, M. Takano, M. Ceretti, C. Ritter, and W. Paulus, Nature **450**, 1062 (2007).

[92] G. Henkelman, A. Arnaldsson, and H. Jónsson, Comput. Mater. Sci. **36**, 354 (2006).

[93] H. Xiang, S.-H. Wei, and M.-H. Whangbo, Phys. Rev. Lett. **100**, 167207 (2008).

[94] J. Pruneda, J. Íñiguez, E. Canadell, H. Kageyama, and M. Takano, Phys. Rev. B **78**, 115101 (2008).

[95] A. D. Franklin and R. B. Campbell, J. Phys. Chem. **59**, 65 (1955).

[96] Y. Kobayashi, Z. Li, K. Hirai, C. Tassel, F. Loyer, N. Ichikawa, N. Abe, T. Yamamoto, Y. Shimakawa, K. Yoshimura, M. Takano, O. J. Hernandez, and H. Kageyama, J. Solid State Chem. **207**, 190 (2013).

[97] M. A. Hayward, M. A. Green, M. J. Rosseinsky, and J. Sloan, J. Am. Chem. Soc. **121**, 8843 (1999).

[98] M. A. Hayward and M. J. Rosseinsky, Chem. Mater. **12**, 2182 (2000).

[99] B. Li, J. Woods, J. Siewenie, H.-Y. Hah, J. A. Johnson, C. E. Johnson, and D. Louca, Chem. Commun. **52**, 2386 (2016).

[100] Y. Zhou, S. Middey, J. Jiang, N. Chen, L. Chen, X. Shi, M. Döbeli, J. Shi, J. Chakhalian, and S. Ramanathan, Appl. Phys. Lett. **107**, 031905 (2015).

[101] J. Shi, Y. Zhou, and S. Ramanathan, Nat. Commun. **5**, 1 (2014).

[102] J. L. García-Muñoz, J. Rodríguez-Carvajal, P. Lacorre, and J. B. Torrance, Phys. Rev. B **46**, 4414 (1992).

[103] S. Yamamoto and T. Fujiwara, J. Phys. Soc. Japan **71**, 1226 (2002).

[104] Y. Maeno, H. Hashimoto, K. Yoshida, S. Nishizaki, T. Fujita, J. G. Bednorz, and F. Lichtenberg, Nature **372**, 532 (1994).

[105] Y. Maeno, S. Nakatsuji, and S. Ikeda, Mater. Sci. Eng. B **63**, 70 (1999).

[106] T. T. Tran, T. Mizokawa, S. Nakatsuji, H. Fukazawa, and Y. Maeno, Phys. Rev. B **70**, 153106 (2004).

[107] S. Ryee, S. W. Jang, H. Kino, T. Kotani, and M. J. Han, Phys. Rev. B **93**, 075125

(2016).

[108] Z. V. Pchelkina, I. A. Nekrasov, T. Pruschke, S. Suga, V. I. Anisimov, and D. Vollhardt, Phys. Rev. B **77**, 046102 (2008).

[109] Q. Huang, J. L. Soubeyroux, O. Chmaissem, I. N. Sora, A. Santoro, R. J. Cava, J. J. Krajewski, and W. F. Peck, J. Solid State Chem. **112**, 355 (1994).

[110] T. Oguchi, Phys. Rev. B **51**, 1385 (1995).

[111] M. Braden, G. André, S. Nakatsuji, and Y. Maeno, Phys. Rev. B **58**, 847 (1998).

[112] A. Kanbayasi, J. Phys. Soc. Japan **41**, 1876 (1976).

[113] W. D. Ryden and A. W. Lawson, J. Chem. Phys. **52**, 6058 (1970).